remote sensing

Article

Automatic Rice Early-Season Mapping Based on Simple Non-Iterative Clustering and Multi-Source Remote Sensing Images

Gengze Wang [1,2], Di Meng [3], Riqiang Chen [1,2], Guijun Yang [1,2], Laigang Wang [4], Hailiang Jin [3], Xiaosan Ge [3] and Haikuan Feng [1,2,5,*]

1 Key Laboratory of Quantitative Remote Sensing in Agriculture of Ministry of Agriculture and Rural Affairs, Information Technology Research Center, Beijing Academy of Agriculture and Forestry Sciences, Beijing 100097, China
2 National Engineering Research Center for Information Technology in Agriculture, Beijing 100097, China
3 School of Surveying and Land Information Engineering, Henan Polytechnic University, Jiaozuo 454000, China
4 Institute of Agricultural Information Technology, Henan Academy of Agricultural Sciences, Zhengzhou 450002, China
5 College of Agriculture, Nanjing Agricultural University, Nanjing 210095, China
* Correspondence: fenghk@nercita.org.cn

Abstract: Timely and accurate rice spatial distribution maps play a vital role in food security and social stability. Early-season rice mapping is of great significance for yield estimation, crop insurance, and national food policymaking. Taking Tongjiang City in Heilongjiang Province with strong spatial heterogeneity as study area, a hierarchical K-Means binary automatic rice classification method based on phenological feature optimization (PFO-HKMAR) is proposed, using Google Earth Engine platform and Sentinel-1/2, and Landsat 7/8 data. First, a SAR backscattering intensity time series is reconstructed and used to construct and optimize polarization characteristics. A new SAR index named VH-sum is built, which is defined as the summation of VH backscattering intensity for specific time periods based on the temporal changes in VH polarization characteristics of different land cover types. Then comes feature selection, optimization, and reconstruction of optical data. Finally, the PFO-HKMAR classification method is established based on Simple Non-Iterative Clustering. PFO-HKMAR can achieve early-season rice mapping one month before harvest, with overall accuracy, Kappa, and F1 score reaching 0.9114, 0.8240 and 0.9120, respectively (F1 score is greater than 0.9). Compared with the two crop distribution datasets in Northeast China and ARM-SARFS, overall accuracy, Kappa, and F1 scores of PFO-HKMAR are improved by 0.0507–0.1957, 0.1029–0.3945, and 0.0611–0.1791, respectively. The results show that PFO-HKMAR can be promoted in Northeast China to enable early-season rice mapping, and provide valuable and timely information to different stakeholders and decision makers.

Keywords: early-season rice mapping; spectral index (SI); synthetic aperture radar (SAR); Simple Non-Iterative Clustering (SNIC); time series filtering; K-Means; Jeffries–Matusita (JM) distance

check for updates

Citation: Wang, G.; Meng, D.; Chen, R.; Yang, G.; Wang, L.; Jin, H.; Ge, X.; Feng, H. Automatic Rice Early-Season Mapping Based on Simple Non-Iterative Clustering and Multi-Source Remote Sensing Images. *Remote Sens.* **2024**, *16*, 277. https://doi.org/10.3390/rs16020277

Academic Editor: Won-Ho Nam

Received: 12 November 2023
Revised: 25 December 2023
Accepted: 5 January 2024
Published: 10 January 2024

1. Introduction

Rice is one of the most important staple food crops in the world [1], accounting for 15% of the major food crop planting area and feeding half of the world's population. It solves the world's hunger problem and is the basis for human survival, social stability, and economic development [2,3].

The traditional rice planting area statistical method is time-consuming and labor-intensive, which is easily affected by subjective factors. It can only summarize the total amount rice planting area, rather than a near-real-time rice spatial distribution map in a large area [4]. Early-season rice mapping refers to rice identification in the early growth stages or before harvest. Near-real-time rice area and its spatial distribution is a prerequisite for rice yield estimation [5], which is of great significance to insurance companies and bulk crop commodity markets [6–8]. In recent years, remote sensing technology has been widely used in crop mapping [9].

Medium-resolution Landsat and Sentinel-2 data are the main optical data sources for rice mapping [10–13]. There have been a lot of studies on rice mapping technology based on optical data, mainly including supervised classification based on rice labels and decision tree classification based on phenology [14]. Supervised classification analyzes the temporal changes in different spectral indices [15], synthesizes the spectral indices according to phenological period or month, and then trains the classification model based on a large number of samples [16,17]. Methods based on phenology often use temporal variation characteristics of spectra in a unique phenological stage, such as the transplanting stage. They selected vegetation index (Normalized difference vegetation index (NDVI), Enhanced vegetation index (EVI), etc.), water index (Normalized difference water index (NDWI), Modified normalized difference water index (MNDWI), Land surface water index (LSWI), etc.), and spectral time series dynamics (mean, standard deviation, max, min, etc.) to distinguish rice and other land cover types with the threshold method [18]. The prominent shortcoming of these methods is that optical images are susceptible to cloud contamination, and it is difficult to synthesize ideal images over a long period. The accuracy of the results depends on the quantity and quality of images during the key phenological stages.

Microwave signals from synthetic aperture radar (SAR) can penetrate clouds and are less affected by weather [19,20]. Therefore, SAR data can obtain regular time-series information during the rice growth season. In addition, SAR is very sensitive to canopy structure and complex dielectric constant. Compared with other crops, rice has unique flooding characteristics during the growth stage, which has been proven to be an effective way for rice monitoring [21]. A time series curve similarity matching method was proposed based on the temporal changes in SAR backscattering intensity during the rice growth period [22], as well as a threshold-based decision tree method relying on its "V"-shaped characteristics before and after the rice transplanting period [23]. These methods have achieved some effective results in some areas [22,23]. However, differences in planting dates, planting patterns, and varieties affect rice radar backscatter intensity during the same period. SAR's sensitivity to soil moisture leads to similar radar backscatter intensity in low-lying drylands, wetlands, and rice. Insufficient time resolution and speckle noise caused by signal fading of Sentinel-1 have become important factors limiting the use of SAR in rice mapping [24].

Meanwhile, the combination of SAR and optical images can improve the accuracy of rice mapping [25]. Instead of a single SAR data source, a combination of optical and SAR is usually applied to traditional machine learning algorithms for crop extraction [22]. Rice mapping based on machine learning of multi-source data often selects percentiles (5%, 25%, 50%, 75%, 95%) during the entire rice growth period or statistics (median, standard deviation, etc.) for each rice phenological stage or monthly synthetic data as features to train classification models [15]. Spectral indices have been widely used in this process. However, the mostly used SAR polarization characteristics are VH, VV, or VH+VV, especially the monthly median synthesized values or the polarization characteristics of the optimal phenological period selected by Jeffries–Matusita (JM) distance [26]. This cannot reflect the changing information of SAR backscattering intensity during the entire rice growth period. At present, there are few studies on the SAR index derived from the calculation of SAR polarization characteristics [27]. A new SAR index needs to be developed, that can reflect the dynamic characteristics of SAR backscattering intensity during the rice growth period [28]. In addition, the traditional pixel-based classification method has a "salt and pepper" phenomenon [29]. Previous studies have shown that the combination of Simple Non-Iterative Clustering (SNIC) based on high-resolution optical images and time-series SAR data can reduce the speckle noise of SAR data and remove speckles in classification results [30].

Supervised classification highly depends on samples to train the classification model [31]. The threshold-based decision tree method needs to rely on samples to find the optimal threshold too. And also the curve similarity matching method needs to provide a standard curve library through samples [22]. The quantity and quality of samples determine the generalizability and reliability of these methods. Some early crop mapping methods use historical crop labels or datasets to predict crop types in the target year through classifier and sample transfer strategies [32,33]. The sample transfer strategy assumes that if the crop type remains unchanged for many years in the same plot, the default target year will also remain unchanged [10]. However, national agricultural policy adjustments may lead to interannual changes in the planting structure, challenging the validity of this assumption. The classifier transfer strategy uses classification model trained by historical crop labels and images directly transferred to the target year [34]. This assumption may not exist when different crop management practices, or any other factors lead to inter-annual variability in spectral and SAR backscatter signal strength [32]. Also, models trained in local environments may not be applicable to other locations [27]. At present, most studies focus on supervised classification or phenology methods to identify rice, and there are fewer studies on unsupervised classification methods [35]. K-Means is a popular and well-known unsupervised classification method, which is widely used in the field of computer vision [36,37].

The major crop datasets in Northeast China have been published [10,38]. They are both crop distribution maps produced after the crops have been harvested. The hysteresis of these datasets reduces their use value in some fields. Moreover, early-season rice mapping can only obtain near-real-time images of the early or middle stages of rice growth. Commonly used curve fitting methods (Double Logistic function (DL), Whittaker Smoother (WS), and The Harmonic Analysis of Time Series (HANTS)) require at least all images of a complete rice growth period or year, so they cannot be used for time series fitting of early-season rice mapping [39,40]. Savitzky–Golay (SG) filtering uses a locally adaptive moving window, and polynomial least squares regression is used within the window to fit time series data [41,42], which can clearly describe small changes in complex crop types and broken plot areas [43]. Linear interpolation based on the most recent valid observations can fill the time gaps [44]. This is often used as the first step of SG filtering in NDVI time series reconstruction to impute missing values [45].

With the support of the Google Earth Engine (GEE) platform, this study proposes a hierarchical K-Means binary classification rice automatic identification method based on phenological information feature optimization (PFO-HKMAR) based on Sentinel-1, Sentinel-2, and Landsat 7/8 data. This method combines multi-source heterogeneous data sources to solve the shortcomings of a single data source, and uses phenology methods to achieve early-season unsupervised automatic mapping of rice. We apply PFO-HKMAR to Tongjiang City, which has strong spatial heterogeneity, and prove the advantages of PFO-HKMAR through accuracy evaluation and comparison with existing crop datasets and ARM-SARFS [10,23,38]. Specifically, the following problems are solved.

(1) How can near-real-time SAR time series data be reconstructed in early-season rice mapping?
(2) Can a SAR index be constructed that can reflect the dynamic characteristics of rice?
(3) What is the earliest date when rice can be identified by PFO-HKMAR?

2. Study Area and Materials

2.1. Study Area

Tongjiang City in the northeastern part of Heilongjiang Province (132–134°E, 47–48°N) was selected as the study area. Tongjiang City locates in the hinterland of the Sanjiang Plain, on the south bank of the confluence of the Heilongjiang River and the Songhua River (Figure 1), with a total area of 6229 km^2. Tongjiang City has a continental monsoon climate with rain concentrated in July and August. The annual average temperature, precipitation, sunshine hours, and frost-free period are 4.5 °C, 709.3 mm, 3504.7 h, and 148 day, respectively.

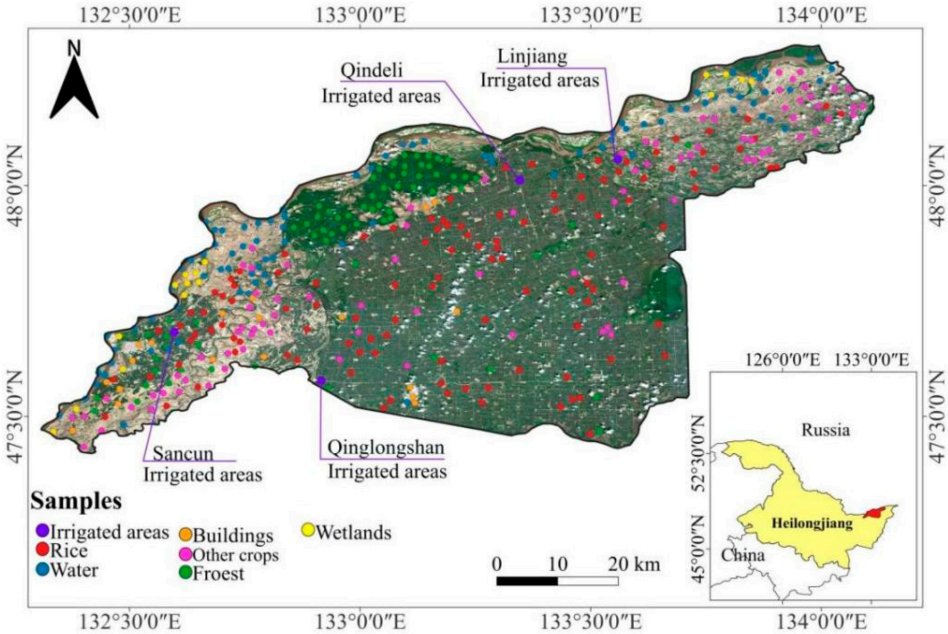

Figure 1. Study area location and sample sites distribution in the Tongjiang City. The background is the true color image of Sentinel-2 on 24 June 2019.

The soil in Tongjiang City is mostly meadow soil, black soil, and white soil, which are suitable for crop cultivation. Tongjiang City plants one-season crops throughout the year, with rice, corn, or soybeans. The central and southern parts of the study area are large farms, mainly producing rice. The western and eastern regions are dominated by small-scale farmers. The crop calendar of some major crops is shown in Table 1. The complex planting structure, diverse planting management methods, and large amounts of wetlands in the study area are representative for PFO-HKMAR evaluation.

Table 1. The crop calendar of main crops in Tongjiang City.

Month	Apr		May			Jun			Jul			Aug			Sep			Oct
Ten-Day	**M**	**L**	**E**	**M**	**L**	**E**	**M**	**L**	**E**	**M**	**L**	**E**	**M**	**L**	**E**	**M**	**L**	**E**
Rice	1	2	2	3	3	4	5	5	5	6	6	7	8	9	10	10	11	12
Soybean			1	2	3	3	4	4	4	5	6	6	6	6	6	6	7	8
Corn			1	2	3	4	4	5	5	5	6	6	7	7	7	7	8	9

Note: Rice: 1, Sowing; 2, Flooding; 3, Flooding/Transplanting; 4, Reviving; 5, Tillering; 6, Boosting; 7, Booting; 8, Heading; 9, Grain filling; 10, Milky maturity; 11, Mature; 12, Harvesting. Soybean: 1, Sowing; 2, Seeding; 3, The third true leaf; 4, Branches forming; 5, Flowering; 6, Pod setting; 7, Mature; 8, Harvesting. Corn: 1, Sowing; 2, Seeding; 3, Three leaves; 4, Seven leaves; 5, Stem elongation; 6, Heading; 7, Milky mature; 8, Mature; 9, Harvesting.

2.2. Datasets and Preprocessing

Due to the incomplete data of Sentinel-1A in the study area, the descending orbit data of Sentinel-1B were selected for SAR data. As shown in Figure 2, the number of remote sensing images under different cloud contents of Landsat 7, Landsat 8, and Sentinel-2 in the study area from January to December 2019 was counted. In April, May, and June, both Sentinel-2 and Landsat 8 were affected by clouds to some extent. Although quality of Landsat 7 images is higher, the "SLC-off" problem is not avoided. To reduce the impact of cloud pollution on optical images and capture rice phenology information more accurately, three types of optical images, Landsat 7/8 and Sentinel-2 were selected. These data are available from GEE.

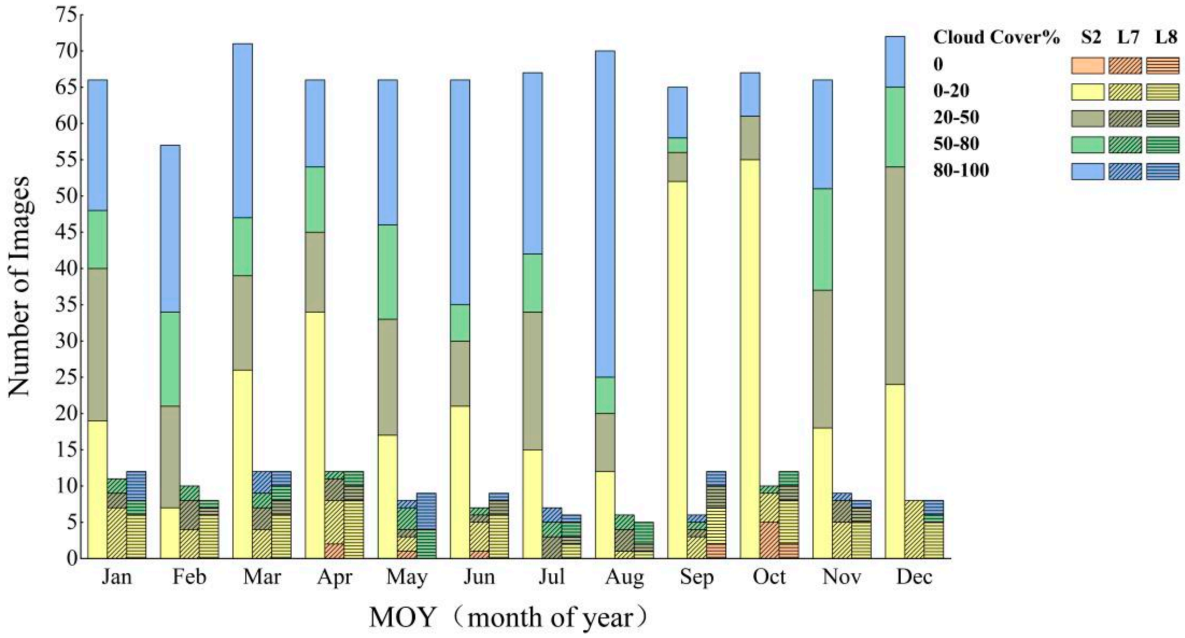

Figure 2. The number of remote sensing images available under different cloud content in the study area for 12 months in 2019. S2, L7, and L8 stand for Sentinel-2, Landsat 7, and Landsat 8.

2.2.1. Sentinel-1/2

Sentinel-1 and Sentinel-2 are an Earth observation mission under the European Space Agency's Copernicus program. The satellite details of Sentinel-1B and Sentinel-2 are shown in Table 2. This study selected the VH polarization method of the descending orbit Sentinel-1B product of the IW mode in 2019 covering the entire study area. The Lee-sigma speckle filtering algorithm of the 7*7 window was used to remove speckle noise [46]. And mosaic the images of the same day to obtain 30 periods of images. Only VH polarization was selected in this study because changes in VH backscattering intensity are more sensitive to rice growth than VV backscattering intensity [47].

Table 2. Sentinel data used in this study.

Sensor	Bands	Wavelength (nm)	Spatial Resolution	Temporal Resolution
Sentinel-2 MSI	Blue	496.6 (S2A)/492.1 (S2B)	10 m	5 d
	Green	560.0 (S2A)/559.0 (S2B)	10 m	
	Red	664.5 (S2A)/665.0 (S2B)	10 m	
	Red Edge 1	703.9 (S2A)/703.8 (S2B)	20 m	
	Red Edge 2	740.2 (S2A)/739.1 (S2B)	20 m	
	Red Edge 3	782.5 (S2A)/779.7 (S2B)	20 m	
	NIR	835.1 (S2A)/833.0 (S2B)	10 m	
	Red Edge 4	864.8 (S2A)/864.0 (S2B)	20 m	
	SWIR 1	1613.7 (S2A)/1610.4 (S2B)	20 m	
	SWIR 2	2202.4 (S2A)/2185.7 (S2B)	20 m	
Sentinel-1B SAR	C (VV)		10 m	12 d
	C (VH)		10 m	

This study used the Sentinel-2 surface reflectance product from 16 April to 15 June 2019, with cloud content less than 80%. The spectral bands with 20 m spatial resolution were resampled to 10 m using the nearest neighbor method. Two methods were used to remove clouds: (1) the Sentinel-2 Cloud Probability product provided by GEE to remove pixels covered by clouds with a threshold of 65%; (2) the QA60 band of the Sentinel-2 image to remove cirrus and dense clouds.

2.2.2. Landsat 7/8

Landsat 7 and Landsat 8 are the seventh and eighth satellites of Landsat. A single satellite can achieve global coverage every 16 days. Landsat 8 is consistent with the previously launched Landsat 7 in terms of spatial resolution and spectral characteristics. The comparison of band information between Landsat 8 and Landsat 7 images is shown in Table 3.

Table 3. Comparison of band information between Landsat 7 and Landsat 8.

Landsat 7			Landsat 8		
Band Name	**Band Range (um)**	**Spatial Resolution**	**Band Name**	**Band Range (um)**	**Spatial Resolution**
Band 1 Blue	0.45–0.52	30 m	Band 1 Coastal	0.433–0.533	30 m
Band 2 Green	0.52–0.60	30 m	Band 2 Blue	0.450–0.515	30 m
Band 3 Red	0.63–0.69	30 m	Band 3 Green	0.525–0.600	30 m
Band 4 NIR	0.77–0.90	30 m	Band 4 Red	0.630–0.680	30 m
Band 5 SWIR1	1.55–1.75	30 m	Band 5 NIR	0.845–0.885	30 m
Band 6 TIR	10.40–12.50	60 m	Band 6 SWIR1	1.560–1.660	30 m
Band 7 SWIR2	2.09–2.35	30 m	Band 7 SWIR2	2.100–2.300	30 m
Band 8 Pan	0.52–0.90	15 m	Band 8 Pan	0.500–0.680	15 m
			Band 9 Cirrus	1.360–1.390	30 m
			Band 10 TIR1	10.6–11.2	100 m
			Band 11 TIR2	11.5–12.5	100 m

Note: NIR, SWIR, and TIR represent near infrared, shortwave infrared, and thermal infrared, respectively.

This study used Landsat 7 and Landsat 8 surface reflectance products with cloud content of less than 80% from 16 April to 15 June 2019. The spatial resolution were resampled to 10 m using the cubic convolution method. The "CFMask" algorithm was used to remove clouds and cloud shadows [48,49].

2.2.3. Ancillary Data

The auxiliary data used in this study are as follows: Crop calendar data in the study area came from the Ministry of Agriculture and Rural Affairs of the People's Republic of China; The European Space Agency (ESA) World Cover 10 m 2020 product (ESAWC2020) provides a global land cover map for 2020 at a 10 m resolution based on Sentinel-1 and Sentinel-2 data; crop mapping datasets (10 m) from 2017 to 2019 (YCP) [38]; and crop mapping datasets (30 m) from 2013 to 2021(XCP) [10]. Data details are shown in Table 4.

Table 4. Download links for related datasets applied in this study.

Datasets	Data Source
Crop calendar of China	https://zdscxx.moa.gov.cn:8080/nyb/pc/calendar.jsp (accessed on 10 August 2023)
ESAWC2020	https://esa-worldcover.org/en (accessed on 12 August 2023)
YCP datasets	https://doi.org/10.6084/m9.figshare.13090442 (accessed on 20 July 2023)
XCP datasets	https://doi.org/10.6084/m9.figshare.20411424.v1 (accessed 20 July 2023)

This study first intersected the cultivated land layer in the ESAWC2020 dataset with the rice layer in the YCP and XCP datasets to obtain a more accurate rice area. The obtained rice area was then superimposed on time-series Sentinel-2 images and high-resolution Google Earth images to create a point sample set and a validation set. A point sample set was mainly used for time-series spectral analysis and calculation of JM distances of different characteristics. We visually interpreted 4201 sample points using the auxiliary data above. Among them, there were 1083 rice plants, 1159 other crops, 505 wetlands, 548 woodlands, 532 buildings, and 374 permanent water bodies. A sample set of plots was mainly used for accuracy verification. There are a total of 98 plots of data, including 50 for rice and 48 for others (including other crops, wetlands, woodlands, buildings, and permanent water bodies). The plot location was first determined through the auxiliary data above, and then the boundaries are delineated through high-resolution Google Earth imagery. The above operations are completed in QGIS.

3. Methods

This study proposed a hierarchical K-Means binary automatic rice classification method based on phenological feature optimization (Figure 3). First, after the reconstruction of Sentinel-1B VH time series backscattering intensity, feature construction and optimization was conducted for data. Then, for optical data, feature selection, optimization, and reconstruction were performed. Finally, the object-based hierarchical K-Means binary classification method was established to automatically identify rice.

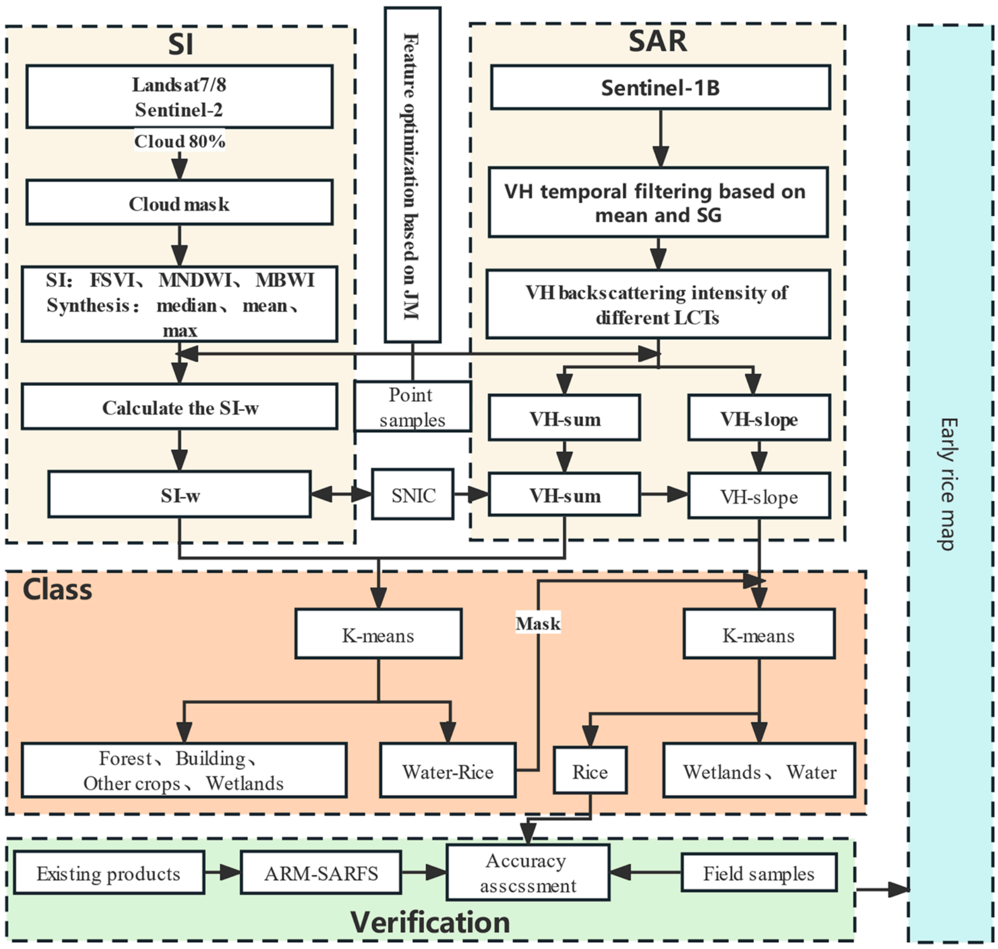

Figure 3. Overview of methodology. Note: LCTs is the abbreviation of "land cover types".

The main steps of PFO-HKMAR were as follows: (1) Use the method combining mean synthesis and SG filtering algorithm to reconstruct the Sentinel-1B SAR time series backscattering data. (2) Construct two SAR features: the cumulative sum of VH backscattering intensity (VH-sum) and the slope of VH backscattering intensity (VH-slope), and determining the best time range through JM distance, so as to calculate VH-sum. (3) Select three spectral indices (SI), namely Flooding signal vegetation index (FSVI), MNDWI, and Multi-Band Water Index (MBWI), for time series image synthesis; generate SI weight overlap map (SI-W) based on best features selected through JM distance. (4) Perform SI-W image segmentation by SNIC method, and obtain the object average value for VH-sum, VH-slope, and SI-W features calculation. (5) Conduct binary classification by the K-Means method using VH-sum and SI-W features, so as to obtain water bodies and rice, including some wetlands, which in this study was called the Water-Rice area. (6) Conduct binary classification through the K-Means method using VH-slope feature and Water-Rice area map to obtain the rice spatial distribution map.

3.1. Reconstruction of the Sentinel-1B Synthetic Aperture Radar Time-Series Backscatter Data

Near-real-time VH curve of rice was constructed by combining mean synthesis and SG filtering. The backscatter intensity of VH was firstly synthesized as a 36-day average to mitigate fluctuations. Secondly, SG filtering was used to obtain the smooth variation trend of the SAR backscattering intensity time series. The length and polynomial order of the SG filter fitting window were set to 5 and 3, respectively. Finally, the last two periods of data missing after SG filtering were filled using the 36-day average and real-time values. This not only weakened the noise that still existed after preprocessing and effectively suppressed the anomalies caused by the environment, thus weakening the differences between rice, but also retained the various characteristics among different land cover types to the greatest extent, which helped realize early-season rice mapping. Figure 4 shows the reconstruction results of rice time series of SAR VH backscattering intensity. Compared with the original VH backscattering curve, the reconstructed one can more clearly reflect the changing trend throughout the whole rice growth.

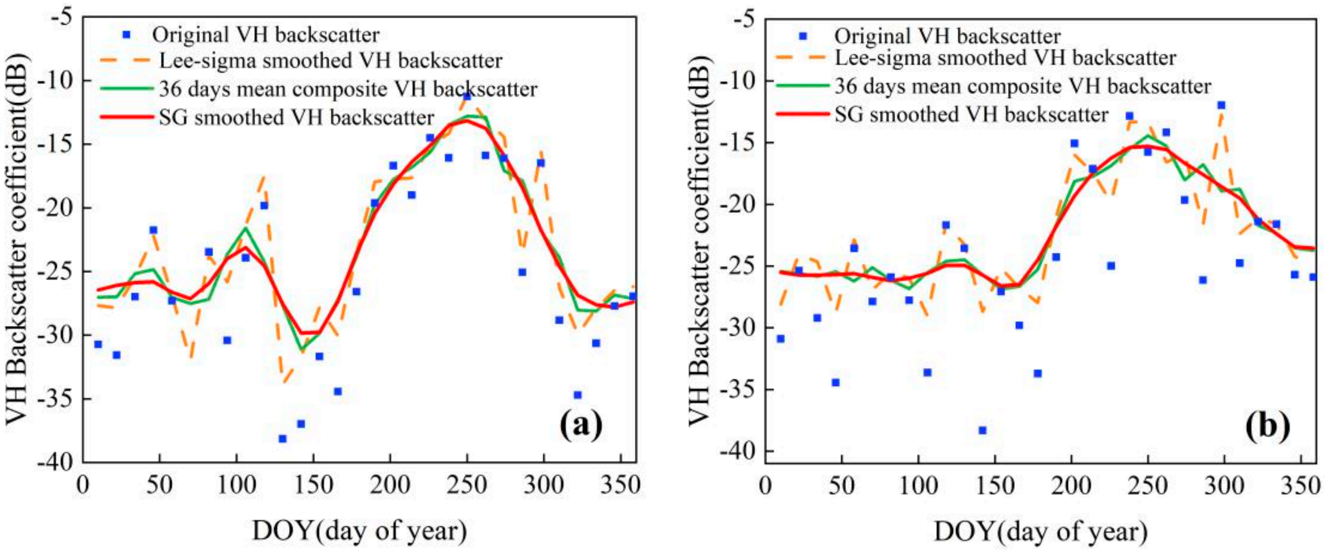

Figure 4. Reconstruction of the sentinel-1B SAR backscatter characteristics time series. (**a**,**b**) represent time series curves at different positions respectively.

3.2. Temporal Signature of Sentinel-1B Backscatter for Different Land Cover Types

Temporal changes in VH backscattering intensity of rice were analyzed based on its biochemical characteristics, which can provide a theoretical basis for a new SAR index constructed in Section 3.3. It can be seen from Figure 5 that different land cover types presented different VH time series curves. According to the curves of rice and its phenology in the study area, three main periods were divided for rice: the sowing and transplanting stage from mid-April to the end of May, which is called the Sowing/Transplanting period (ST); the Transplanting/Mature period (MT) from early June to August, which covers rice growth stages of reviving, tillering, jointing, and heading; the Mature/Harvest period (MH) from early September to October including rice growth stages of Milky maturity, Mature, and harvesting. During the entire growth period of rice, the VH backscattering intensity of forest and buildings is greater than that of rice. And water performed oppositely.

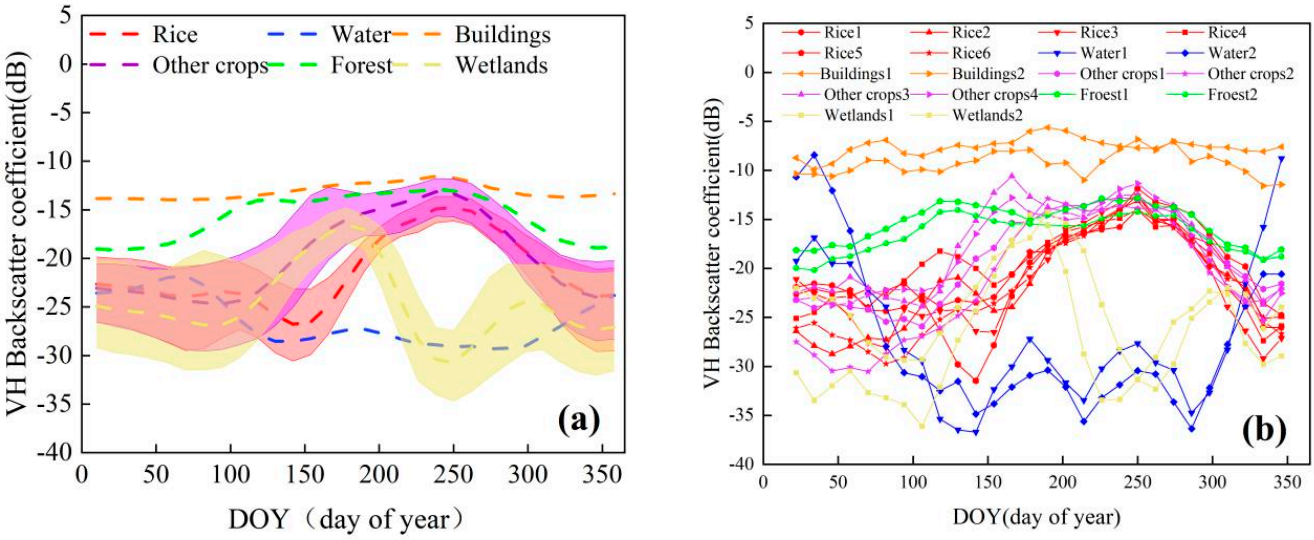

Figure 5. VH backscattering intensity of different land cover types in the study area in 2019. (**a**) The dashed lines represent the average, and the error bars represent the percentile 5% and 95%. (**b**) Typical VH backscatter intensity curves of different land cover types in the study area.

In the ST stage, the humidity of rice field gradually increases, with a decrease in roughness. The specular reflection of water in rice field is the main backscattering mechanism, which causes the SAR backscattering intensity dropping rapidly from about −23 dB to about −26 dB (the lowest value). As shown in Figure 5b, there are large differences in the VH curves during the ST stage of rice. Rice 1–4 have a "V"-shaped characteristic with obvious flooding signals before and after the transplanting period. This is called the "standard rice time series curve" (SR). Rice 5–6, on the contrary, demonstrate what is called the "non-standard rice time series curve" (NSR). The VH backscattering intensity of NSR may be greater than that of other crops and wetlands.

During the MT stage, the SAR backscattering intensity increases from approximately −26 dB to approximately −14 dB (the highest value). During this period, the VH backscattering intensity of rice has been lower than that of other crops. In early June, rice is in the greening and tillering stage. During this period, rice is sparsely distributed, rice seedlings are young, and the water content of rice fields is high, with water accounting for the majority. Therefore, the VH backscattering intensity is dominated by specular reflection, with less body scattering and Double Bounce. During this period, the VH backscattering intensity was still low but began to gradually increase. From the end of June to the end of July, rice is mainly in the late tillering and jointing stages. During this period, the number of rice tillers increases, the rice grows rapidly, and the canopy roughness gradually increases. The main backscattering intensity of VH becomes the body scattering of rice and the Double Bounce between the rice stem and the lower surface of the rice field. The specular reflection of the rice field water gradually decreases, causing the VH backscattering intensity to increase rapidly. In August, rice is mainly in the reproductive stage. During this period, the rice plant height reaches its highest, the leaves almost completely cover the water surface of the rice field, and the rice biomass is the highest. The main backscattering intensity of VH is the body scattering of rice and the surface scattering of the rice canopy. The Double Bounce decreases and the VH backscattering intensity gradually reaches the maximum [50]. During this period, due to the arrival of the rainy season, precipitation gradually increases, and the VH backscattering intensity of the wetland decreases rapidly. The VH backscattering intensity of rice is greater than that of wetland. After September, rice gradually matures and is harvested. During this period, the water content of rice leaves decreases, the rice ears bend, the leaves gradually turn yellow, and the VH backscattering intensity of the rice fields continues to decrease.

3.3. Feature Construction

This study used two feature types: (1) SAR index derived by analyzing the temporal changes in VH backscattering intensity of different land cover types. (2) Spectral index generated from optical spectral calculation based on existing research.

3.3.1. SAR Feature

By analyzing VH time series changes in different land cover types, this section proposed two new SAR characteristics: the cumulative sum of VH backscattering intensity for a specific time period (VH-sum) and the VH slope in the rice growth stage.

According to the temporal dynamics of VH backscattering intensity of rice in Section 3.2, in the ST stage, NSR does not have obvious "V"-shaped characteristics, and the VH backscattering intensities of rice, wetland, and other crops intersect. In the MT stage, the VH backscattering intensities of SR and NSR were lower than those of other crops. Before the arrival of the rainy season in the MT stage, the VH backscattering intensity of wetlands is higher than that of rice, indicating that the impact of wetlands on rice can be effectively removed at this stage. Considering the above issues, to highlight these characteristics, this study proposed the cumulative sum of VH backscattering intensity. Through the accumulation of VH backscatter intensity, subtle differences can be exaggerated, improving the separability of rice and other crops, while reducing intra-class differences in rice. During the rice growth period, the VH-sum of buildings, woodland, and other crops is greater than that of rice, the VH-sum of water bodies is smaller than that of rice, and the VH-sum of wetlands fluctuates with rainfall.

Recent studies have shown that using radar backscatter slope is effective for rice classification [23,51]. Although the VH slope of rice during the growth stage is close to that of other crops, it is highly separable from buildings, forest land, and water bodies. In this study, the VH slope of rice was obtained by linear fitting of the VH backscatter intensity and time of multiple images after 16 May 2019.

3.3.2. SI Feature

Compared with other crops, a unique physical characteristic of rice is that rice needs to grow in flooded soil [52]. This study selected FSVI (a combination of NDVI and LSWI), MNDWI, and MBWI to identify water information in the early stages of rice growth. These spectral indices have been widely used in rice mapping and have been proven to be effective. When rice is in the transplanting and tillering stages, the LSWI of rice field is greater than NDVI. Therefore, the FSVI, calculated by subtracting NDVI from LSWI (in this study, the maximum value of NDVI was selected during the period from 16 April to 15 May 2019), can highlight the water body information in rice fields and avoid vegetation interference on LSWI identification of water bodies. MNDWI can reduce the background effects caused by vegetation and soil and highlight water body information [53]. MBWI can robustly extract surface water from cluttered backgrounds such as mountainous shadows and dark built-up areas. At the same time, the seasonal effects caused by changes in solar conditions can be reduced [54]. The band operations of FSVI, MNDWI, and MBWI are shown in Table 5.

Table 5. Five spectral indices were selected in this study and their associated equations.

Spectral Index	Equation	Reference
NDVI	$(\rho\mathrm{NIR}-\rho\,\mathrm{Red})/(\rho\mathrm{NIR}+\rho\,\mathrm{Red})$	[55]
LSWI	$(\rho NIR-\rho SWIR1)/(\rho NIR+\rho SWIR1)$	[52]
FSVI	$LSWI-NDVI$	[56]
MNDWI	$(\rho Green-\rho SWIR1)/(\rho Green+\rho SWIR1)$	[53]
MBWI	$2*\rho Green-\rho\mathrm{Red}-\rho NIR-\rho SWIR1-\rho SWIR2$	[54]

3.4. Feature Optimization and Weighted Superposition

JM distance was used to evaluate the separability of VH-sum and VH-slope in different time ranges and select the best rice phenological phase construction characteristics. By analyzing the separability of spectral indices, a spectral index weighted overlay map during the rice flooding period was constructed.

Although using more features is beneficial for detecting subtle differences between different land cover types, the participation of redundant features may reduce classification efficiency and accuracy to a large extent [57]. Spectral separability is an important factor in determining rice classification accuracy. In land cover classification, JM distance is a widely recognized spectral separability measure [58]. This study used JM distance to quantitatively analyze the separability of rice and non-rice in different phenological stages. The calculation formula of JM distance can be found in [57].

3.4.1. SAR Feature Separation Evaluation

The JM distance was employed in this study to assess the discriminability of various land cover types based on VH-sum characteristics across different temporal intervals. As shown in Figure 5, different land cover types showed different characteristics in different phenological stages. Therefore, separability evaluation was performed on VH-sum features at different time intervals with different starting dates. Since the time resolution of Sentinel-1B is 12 d, the time interval was selected as half a month. The specific time interval design was shown in Table 6. The rice transplanting dates in the study area are mainly concentrated in mid-May, and then as the rice grows, the VH backscattering intensity of the rice gradually increases. This study used 15 May as the starting date and 1 month as the time interval to evaluate the separability of different land cover types in VH-slope characteristics in different time ranges.

Table 6. Different time intervals in different start date time phases in 2019.

End Date	**Start Date**								
	1 May	**16 May**	**1 June**	**16 June**	**1 July**	**16 July**	**1 August**	**16 August**	**1 September**
Name	SART1	SART2	SART3	SART4	SART5	SART6	SART7	SART8	SART9
15 May									
31 May									
15 June									
30 June									
15 July									
31 July									
15 August									
31 August									
15 September									
30 September									

In terms of VH-sum characteristics, when the starting date is 1-June, the separability of rice and other land cover types is the best (Figure 6). VH-slope characteristics can effectively improve the separability of rice and water. It can also make up for the poor separability of VH-sum characteristics on rice and wetland in rainy season. Therefore, the VH-sum feature was studied in the SART3 stage (Table 6).

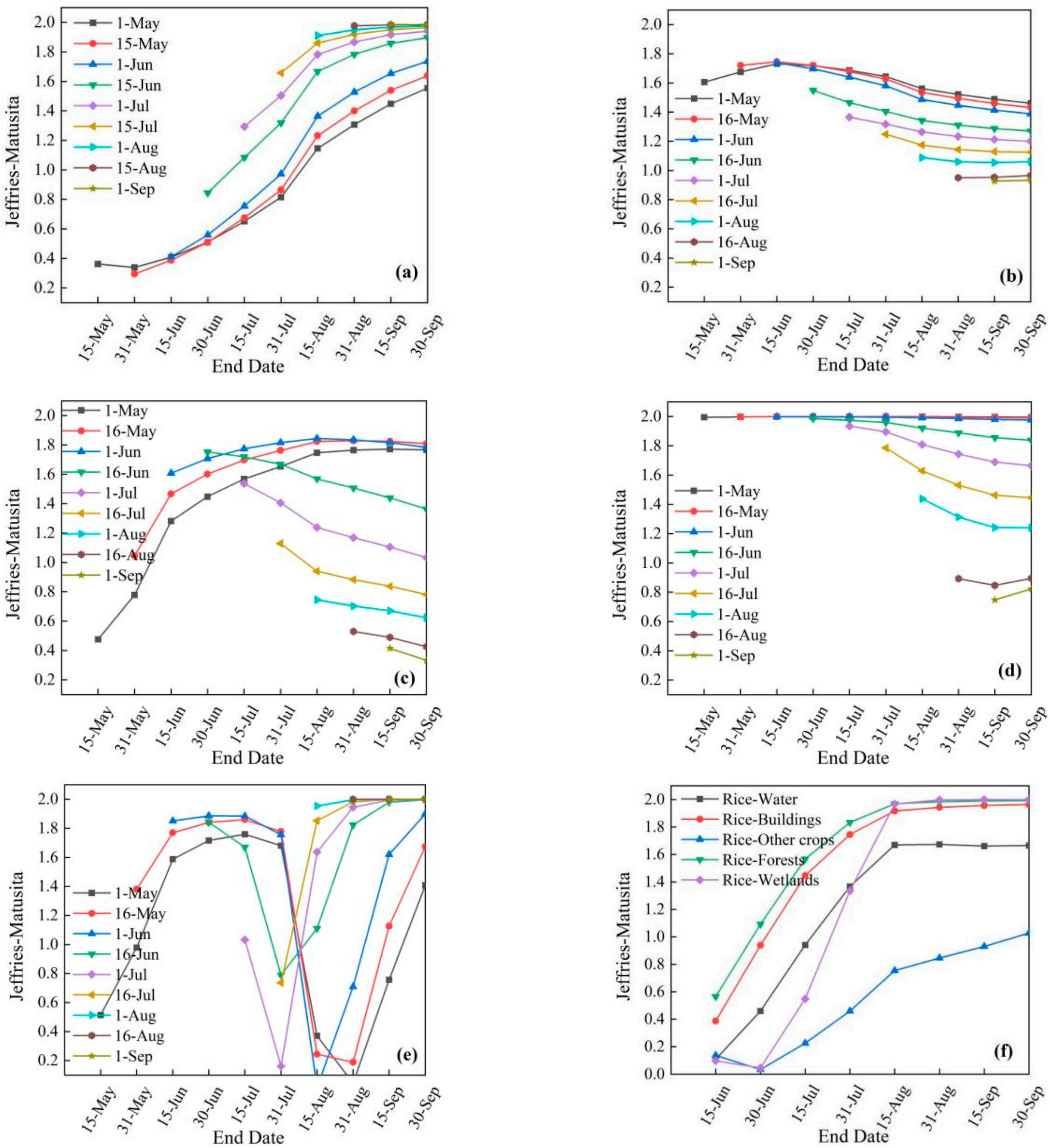

Figure 6. JM distance with different characteristics of different land cover types. (**a**–**e**) These indicates the JM of the VH-sum feature at different times. (**a**–**e**) These represent the JM distance of Rice-Water, Rice-Buildings, Rice-Other crops, Rice-Forests, and Rice-Wetlands. Image (**f**) shows the JM distance of the VH-slope feature in SART2. (**a**–**e**) For legends, refer to Table 6.

3.4.2. SI Feature Optimization and Weighted Superposition

Three optical data sources were selected in this study: Landsat 7/8 and Sentinel-2. Three spectral indices, namely FSVI, MNDWI, and MBWI, and their average, maximum, and median value were obtained for image synthesis. Finally, the optimal features were selected through JM distance for weight overlap addition to obtain the weight overlap addition map of SI. The details are as follows:

(1) Multiple methods for image synthesis.

The time range for identifying flooding signals in the early growth stage of rice was determined as 16 April to 15 June 2019. The time range is guaranteed to be at least 30 days and accumulated in half-month intervals, divided into 6 time stages [34]. Perform median synthesis, maximum synthesis, and average synthesis on the images within the time period, respectively [34,59]. The time stages in 2019 are defined as follows: 16 April~15 May (SIT1), 16 April~31 May (SIT2), 16 April~15 June (SIT3), 1 May~31 May (SIT4), 1 May~15 June (SIT5), 16 May~15 June (SIT6).

(2) Feature selection and weight overlap based on JM distance.

Analyze the JM distances of rice and other crops using different synthesis methods with different spectral indices in different periods (Figure 7). In the SIT5 stage, the spectral separability of the mean synthesis and median synthesis of FSVI and MNDWI is optimal. The median synthesis of MBWI (MBWI-median) obtained the highest JM distance of 1.93 in the SIT3 stage.

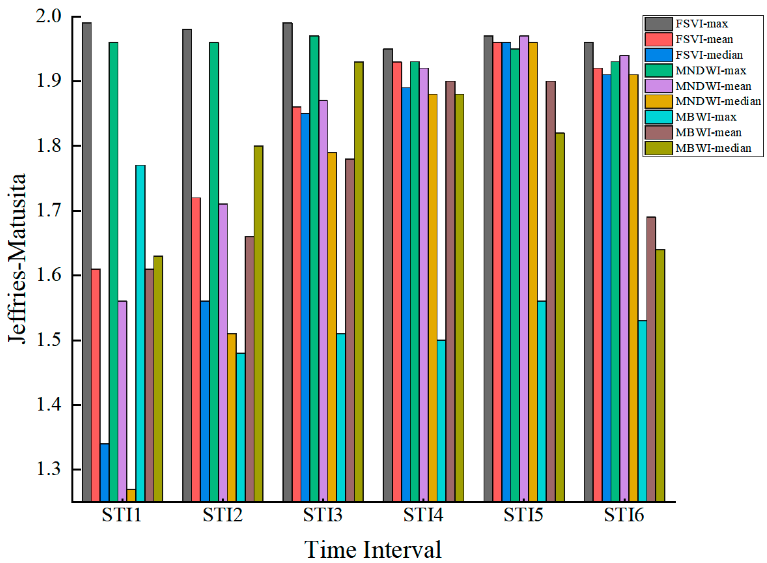

Figure 7. JM distance values of rice and other crops at different time intervals by different synthesis methods and different spectral indices.

Based on the above analysis, this study first selected the maximum composite of FSVI (FSVI-max-SIT5), the average composite of FSVI (FSVI-mean-SIT5), and the median composite of FSVI (FSVI-median-SIT5) in the SIT5 stage for weighted overlap to obtain the weighted overlapped value of FSVI (FSVI-W). Then select the maximum synthesis of MNDWI (MNDWI-max-SIT5), the average synthesis of MNDWI (MNDWI-mean-SIT5), and the median synthesis of MNDWI (MNDWI-median-SIT5) in the SIT5 stage to perform weight overlap addition, and obtain the weight overlap addition value of MNDWI (MNDWI-W). Finally, weight overlap addition was performed on FSVI-W, MNDWI-W, and MBWI-median-SIT3 to obtain the SI-W. Since the JM distance of different features are relatively close, this study chose the average weight. SI-W is calculated as follows:

$$\text{FSVI-W} = \text{FSVI-max-SIT5} \times \text{W1} + \text{FSVI-mean-SIT5} \times \text{W2} + \text{FSVI-median-SIT5} \times \text{W3}$$

$$\text{MNDWI-W} = \text{MNDWI-max-SIT5} \times \text{W4} + \text{MNDWI-mean-SIT5} \times \text{W5} + \text{MNDWI-median-SIT5} \times \text{W6}$$

$$\text{SI-W} = \text{FSVI-W} \times \text{W7} + \text{MNDWI-W} \times \text{W8} + \text{MBWI-median-SIT3} \times \text{W9}$$

3.5. Superpixel Segmentation Based on Simple Non-Iterative Clustering

SNIC algorithm in GEE was used to perform SI-W segmentation. The SNIC algorithm does not require iterative convergence of cluster centers [60,61]. It requires forced connections from the beginning of algorithm clustering. It takes up less memory and is faster. It is suitable for images of different sizes and resolutions. Considering the texture characteristics of landscape patches in the study area and previous studies [30], this study tested the spacing of superpixel seeds from 20 to 100 at intervals of 5 and finally selected 40. SNIC, in GEE, requires setting some main parameters, these parameters were set as follows: compactness = 0, connectivity = 8, and neighborhood size = 1000.

3.6. K-Means Model

The purpose of K-Means is to cluster the dataset by quantifying the similarity among samples, aiming to minimize intra-class gap and maximize inter-class gap [62,63]. Considering the performance of VH-sum, VH-slope, and SI-W characteristics for different land cover types, as well as the deficiencies of K-Means clustering algorithm, a hierarchical K-Means binary classification algorithm was proposed. For detailed steps, please refer to Table S4 in the Supplementary Materials.

3.7. Determining Earliest Identifiable Timing (EIT)

Through the JM distance analysis of the separability of various characteristics of different land cover types, the SART3 time stage was selected, with the starting date being 1 June 2019, and gradually extending until 30 September 2019, at half-month intervals. The PFO-HKMAR was employed to identify rice in different stages, and an accuracy evaluation was conducted. The determination of EIT was based on an examination of temporal changes and spatial distribution pertaining to rice mapping accuracy.

3.8. Accuracy Assessment

To prove the reliability of rice distribution in the study area, the accuracy of rice classification was evaluated and the consistency of its spatial distribution was verified. Five evaluation indices, including overall accuracy (OA), producer accuracy (PA), user accuracy (UA), kappa coefficient (KC), and F1 score (F1), were calculated by establishing a confusion matrix to quantitatively assess the mapping results [58]. A detailed description of these five indicators can be found in previous studies [16,58]. We compared our results with existing YCP and XCP datasets. Furthermore, we compared our findings with the ARM-SARFS method proposed by Zhan et al. [23], which is based on the "V"-shaped characteristics before and after the rice transplanting period. The choice to compare with ARM-SARFS was motivated by its status as a classic rice recognition algorithm using Sentinel-1 data that has attracted widespread attention.

4. Results

4.1. Comparative Analysis of Early-Season Rice Mapping Based on SNIC and Pixel

The changes in the accuracy of rice mapping based on SNIC and pixel-based multi-source remote sensing images are shown in Figure 8. Regardless of the combination of SAR+SI or SAR, the classification accuracy based on SNIC is higher than that based on pixels. The combined SNIC-based classification of SAR+SI is 0.0478, 0.0932, and 0.0530 better than the pixel-based classification OA, KC, and F1, respectively. The SNIC-based classification of SAR is improved by an average of 0.0511, 0.0993, and 0.0584 compared to the pixel-based classification OA, KC, and F1, respectively. Based on the SNIC classification, as shown in Figure 8, it can be observed that regardless of the SAR+SI combination or only SAR, the F1 change trend exhibits a rapid increase before 15 July, followed by a slower increase thereafter. It shows a slight increase after 15 August and eventually reaches a state of almost stabilization. The pixel-based classification increased rapidly until 15 August, then it slightly increased and almost stabilized. This indicates that in early-season rice mapping, SNIC-based classification has more advantages than pixel-based classification.

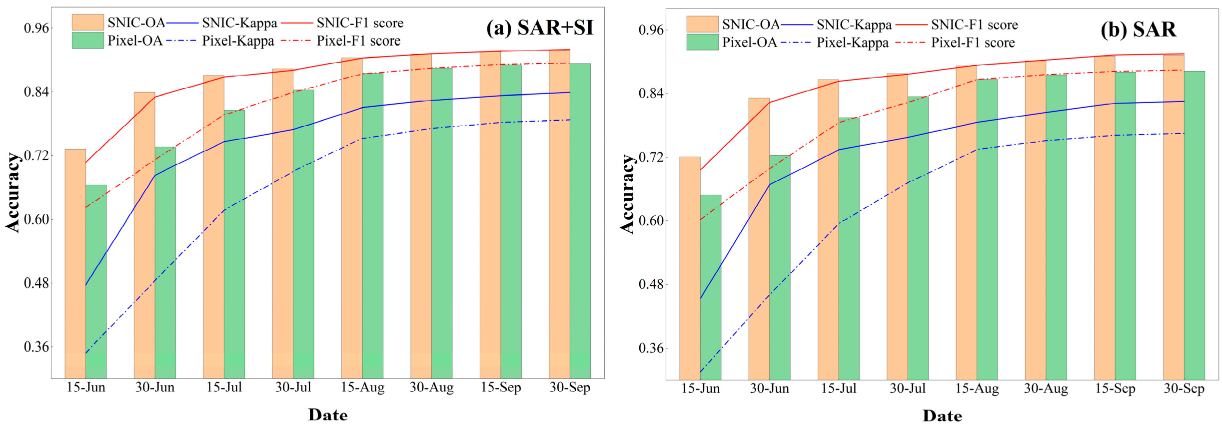

Figure 8. OA, Kappa, and F1 scores for rice classification based on SNIC and pixel at different time intervals of the SART3 time stage from different remote sensing image data sources.

4.2. Effect of Different Data Sources on the Early-Season Rice Mapping

The changes in rice mapping accuracy for different combinations of data sources are shown in Figure 9. Whether it is SNIC-based or pixel-based classification, the combination of SAR+SI yields higher classification accuracy than using SAR alone. In the SNIC-based classification, the combination of SAR+SI improves OA, KC, and F1 by an average of 0.0081, 0.0165, and 0.0071, respectively, when compared to using SAR only. In the pixel-based classification, the combination of SAR+SI improves OA, KC, and F1 by an average of 0.0114, 0.0227, and 0.0124, respectively, compared to using SAR only. Compared with the SNIC-based classification method, the pixel-based classification method has a greater accuracy improvement through the combination of SAR+SI than using only SAR data. It can be observed from the changes in F1 in Figure 9 that in different phenological stages of rice, the combination of SAR+SI can stably improve the accuracy of rice mapping compared with only using SAR, and has little impact on early-season rice mapping.

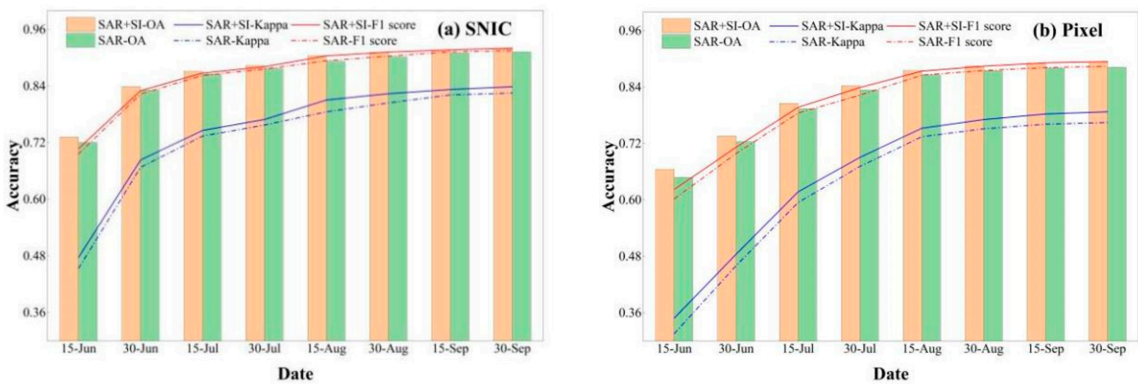

Figure 9. Comparison of OA, Kappa, and F1 scores of rice classification based on multi-source remote sensing images at different time intervals in the SART3 time stage. (**a**) Rice classification based on SNIC; (**b**) pixel-based rice classification.

4.3. The Earliest-Identified Temporal and Spatial Distribution of Rice

Based on the analysis in Sections 4.1 and 4.2, this study chooses the combination of SNIC-based SAR+SI to determine the final EIT. Existing research has defined the earliest identifiable time of each crop as the first time the F1 of the crop reaches 0.9 [34]. Although the F1 of rice is verified by accuracy to be greater than the threshold 0.9 on 15 August, after all, the accuracy verification is carried out with limited samples. We determined the earliest date of rice identification by analyzing the spatial distribution map of rice after 15 August (inclusive). From the spatial distribution of rice in the study area shown in Figure 10, we can observe a generally consistent spatial distribution of rice at different time intervals in the study area, with the main difference being observed in the Qinglong River area. It can be observed from the detailed map of the Qinglong River area in Figure 10 that although the F1 of rice is greater than 0.9 on 15 August, the Qinglong River channel is incorrectly identified as rice. The rice recognition effect on 31 August is the best, even better than that of 15 September and 30 September. However, some dunes in the river channel will still be mistakenly classified as rice. Based on the temporal changes in F1 in rice and the spatial distribution of rice, this study selected 31 August as the earliest identifiable date of rice. The results based on the PFO-HKMAR method in the following analysis of this study refer to the rice identification results of the SNIC-based SAR+SI combination at the SART3 time stage on 31 August.

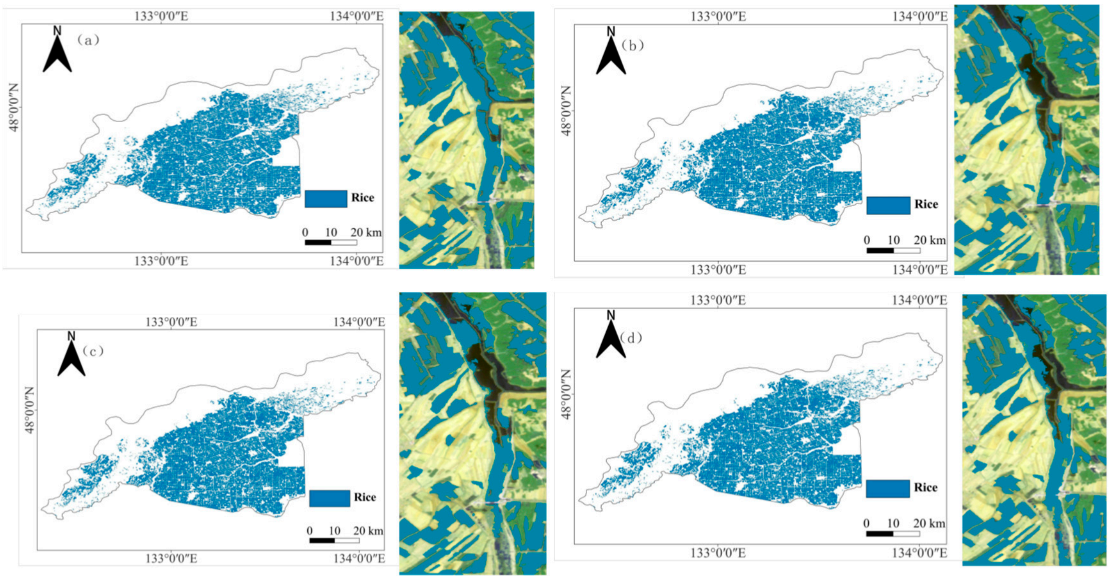

Figure 10. The spatial distribution map of rice in the study area on 15 August, 31 August, 15 September, and 30 September in the SART3 period and the local detailed map of the Qinglong River area. Image (**a**–**d**) represent 15 August, 31 August, 15 September, and 30 September respectively. The bottom image is Sentinel-2 on 24 June 2019 (R: SWIR2, G: SWIR1, B: NIR).

The rice planting area in Tongjiang City in 2019 is approximately 3651.29 km^2. As shown in Figure 10, rice is primarily distributed in large farms located in the central region. It is then followed by the Sancun Irrigation District along the Heilongjiang and Songhua Rivers to the west, and scattered in the Linjiang Irrigation District in the northeast. This is consistent with the actual situation in the study area.

4.4. Comparison of Rice Mapping Results between PFO-HKMAR and ARM-SARFS

ARM-SARFS is an unsupervised classic rice identification method based on rice phenology. Therefore, we compared PFO-HKMAR and ARM-SARFS in terms of accuracy and spatial distribution. The rice mapping method of ARM-SARFS is detailed in [23]. We set the thresholds of slope (MRsowing-transplanting), slope (MRgrowing), mean (VHyear), and mean (VHrice-growth) to 0, 0, −20 dB, −20 dB, respectively. These are general thresholds adapted to the Northeast region. As shown in Table 7, PFO-HKMAR is 0.1957, 0.3945, and 0.1791 higher than ARM-SARFS in OA, KC, and F1, respectively. As shown in Figure 11, ARM-SARFS performs better in large farm areas, but the extracted rice plots are broken. The phenomenon of missing mention is observed in small farmer economic areas. Additionally, the water bodies of Heilongjiang, Songhua River, and Qinglong River are mistakenly classified as rice fields. Furthermore, there are also a large number of broken patches in forest land that are misdivided into rice. However, there is no misdividing of wetlands into rice in the Yalu River and Nongjiang River basins.

Table 7. Rice classification accuracy of YCP datasets, XCP datasets, and ARM-SARFS method.

Accuracy	UA	PA	OA	Kappa	F1
ARM-SARFS	0.7511	0.7155	0.7157	0.4295	0.7329
YCP	0.9089	0.7998	0.8607	0.7211	0.8509
XCP	0.7164	0.8837	0.8248	0.6431	0.7913

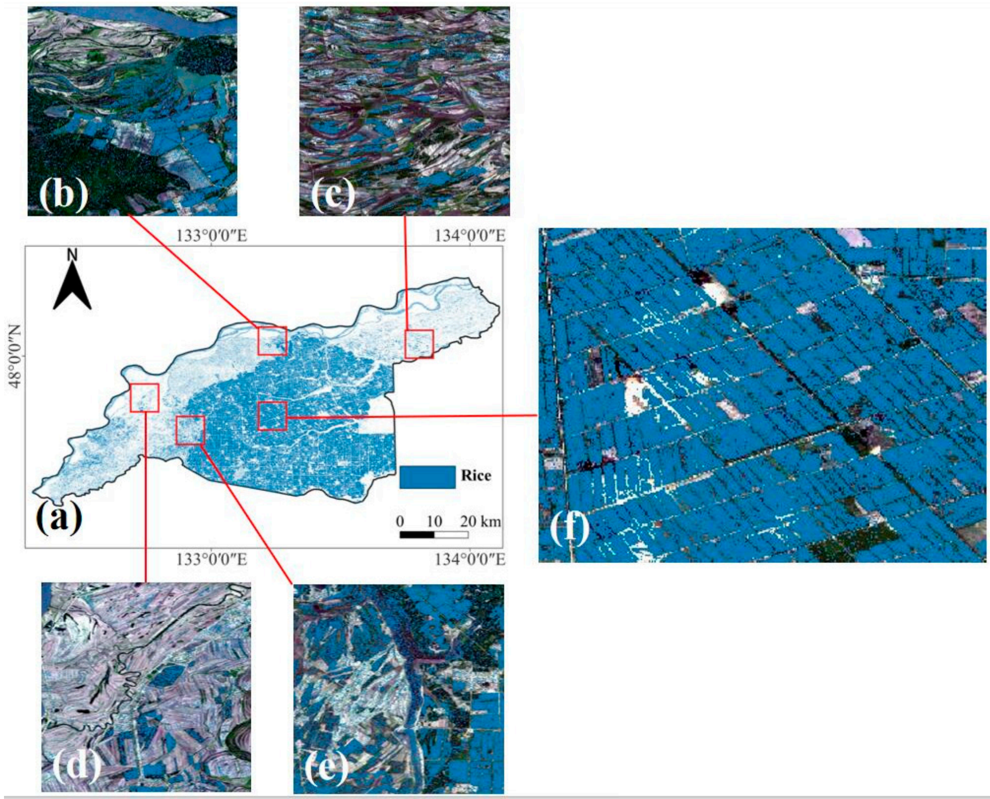

Figure 11. Rice spatial distribution map and local detail map of ARM-SARFS. (**a**) Tongjiang City; (**b**) Heilongjiang Basin; (**c**) Yalu River Basin; (**d**) Songhua River Basin; (**e**) Qinglong River Basin; (**f**) Qinglongshan Farm. The bottom image is Sentinel-2 on 24 June 2019 (R: red; G: green; B: blue).

4.5. Comparison between PFO-HKMAR and Existing Rice Datasets

We compare PFO-HKMAR with the recently publicly released medium-resolution rice datasets of YCP and XCP in terms of accuracy and spatial distribution. As shown in Table 7, PFO-HKMAR is 0.0507, 0.1029, and 0.0611 higher than YCP in OA, KC, and F1, respectively. PFO-HKMAR is 0.0866, 0.1809, and 0.1207 higher than XCP in OA, KC, and F1, respectively. Figures 12 and 13 indicate that the spatial distribution of rice in YCP and XCP is generally consistent with the spatial distribution of rice in PFO-HKMAR, but there are differences in some regions. The PFO-HKMAR method and the YCP datasets provide more detailed field information. The XCP datasets only use 30 m Landsat data. Due to mixed pixels, the field roads are misdivided into rice. The YCP datasets mainly misclassify large wetlands in the Yalu River and Qinglong River basins as rice fields. The XCP datasets mainly misclassify large wetlands in the Heilongjiang and Songhua River basins as rice fields. Moreover, there are a small number of broken patches distributed in the study area, and depressions and wetlands are misidentified as rice. Compared to the datasets of YCP and XCP, PFO-HKMAR exhibits the best distinction between rice and wetland without any broken spots.

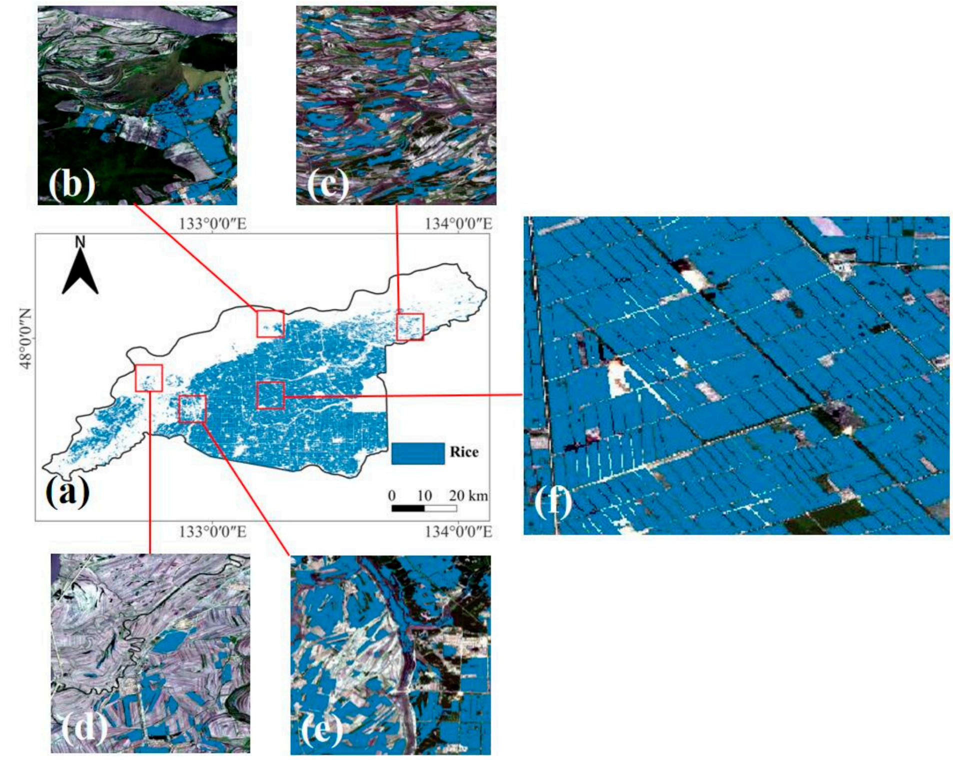

Figure 12. Rice spatial distribution map and local detail map of YCP. (**a**) Tongjiang City; (**b**) Heilongjiang Basin; (**c**) Yalu River Basin; (**d**) Songhua River Basin; (**e**) Qinglong River Basin; (**f**) Qinglongshan Farm. The bottom image is Sentinel-2 on 24 June 2019 (R: red; G: green; B: blue).

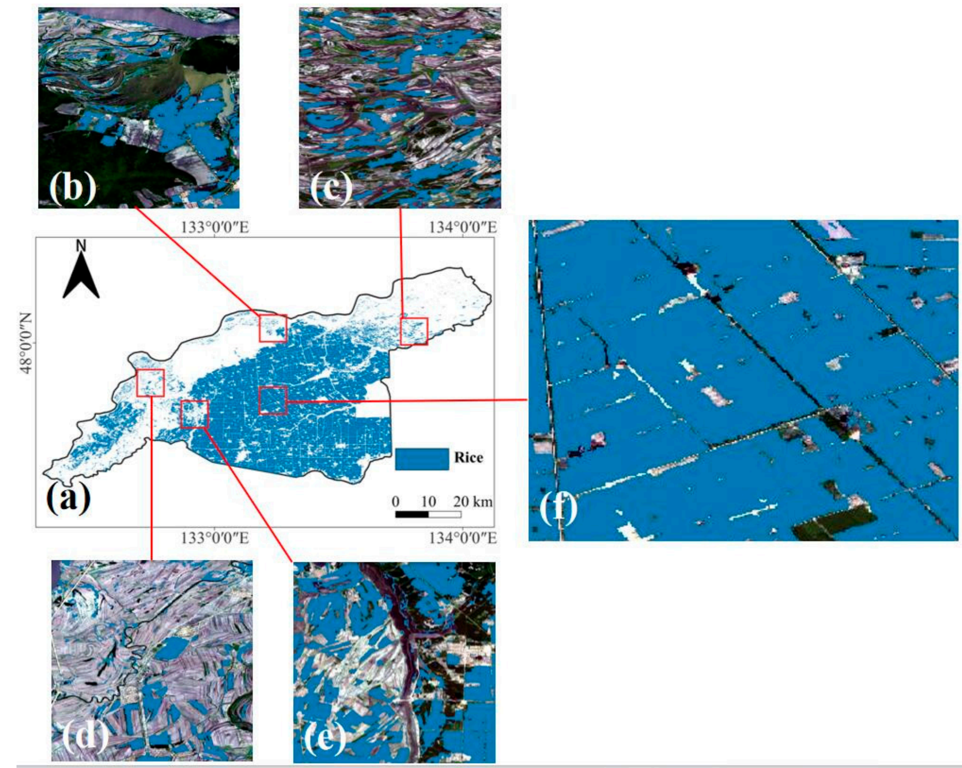

Figure 13. Rice spatial distribution map and local detail map of XCP. (**a**) Tongjiang City; (**b**) Heilongjiang Basin; (**c**) Yalu River Basin; (**d**) Songhua River Basin; (**e**) Qinglong River Basin; (**f**) Qinglongshan Farm. The bottom image is Sentinel-2 on 24 June 2019 (R: red; G: green; B: blue).

5. Discussion

5.1. Feasibility of an Unsupervised Early-Season Rice Mapping Approach Based on Phenology

The feasibility of K-Means classification based on phenology in early-season rice mapping is analyzed in this section, considering the VH temporal changes in rice and the JM distance of different characteristics. We use a K-Means clustering model to automatically learn multi-feature temporal change information of different land cover types based on phenology information. It does not require a large number of samples to train the model, nor does it need to find the optimal segmentation threshold, and it overcomes the shortcomings of K-Means classification. The method can automate rice mapping and achieve good results in early-season rice mapping. Additionally, it can also be extended to identify other crops.

The PFO-HKMAR method based on the combination of SAR+SI can identify rice in the study area as early as the end of August. It can be observed from the time series changes in VH backscattering intensity of different land cover types that the VH backscattering intensity of other crops is significantly greater than the VH backscattering intensity of rice from June to July. Although the VH backscattering intensity of other crops overlapped with the VH backscattering intensity of rice in August, the average VH backscattering intensity of other crops is still greater than the average VH backscattering intensity of rice. In early September, the VH backscattering intensity of both reaches the maximum and then begins to decrease. During this period, the VH backscattering intensity of both is almost the same. It shows that before September, rice and other crops can be better separated by using VH-sum characteristics. The VH-sum features of rice and other crops are separable well on 15 August and 31 August, and the JM distance values are 1.8444 and 1.8350, respectively. Before September, the VH backscattering intensity of buildings and woodland is much higher than that of rice, so the separation of rice and buildings, and rice and woodland can be easily achieved through the VH-sum feature. Since rice and wetland have flooding signal asynchrony in the early stages of rice growth, VH-sum and SI-W features can easily distinguish rice and wetland at this stage. After that, as the precipitation gradually increased, on 15 August, the JM distance between rice and wetland in the VH-sum feature is almost 0. However, the JM distance between rice and wetland in the VH-slope feature reaches 1.99. Therefore, before September, according to the performance of VH-sum, VH-slope, and SI-W characteristics in different phenological stages, the advantages of the three complement each other at different time intervals, and effective early separation of rice and wetland can be achieved. Although the VH backscatter intensity of the water body fluctuates depending on the water level, as the rice grows, the separability of the two gradually increases. Regarding the VH-slope feature, the JM distance between rice and water reaches saturation on 15 August, with a value of 1.6693. Therefore, the temporal changes in different land cover types illustrate that rice can be identified at the end of August.

5.2. Comparison of Rice Classification Based on SNIC and Pixel

This section discusses the advantages of using SNIC in the PFO-HKMAR method from the perspective of rice mapping accuracy and comparison with other datasets. The quality of the image affects the segmentation effect of SNIC, and the segmentation effect has a decisive impact on rice recognition. Research has shown that multi-stage NDVI segmentation is superior to using a single image [64]. We choose SI-W images to search for homogeneous objects, which can identify rice fields more accurately. And, it is more suitable for image segmentation than using a single spectral index or solely relying on the median synthesis method.

The study found that the classification results based on SNIC are superior to those based on pixels, whether it involved a combination of SAR+SI or using only SAR data. This is mainly because the average value of all pixels within the object is used to reduce the speckle effect of SAR. By smoothing the pixel values of the same crop within the object in the same plot, it reduces the intra-class variance of different land cover types and increases the separability between different land cover types. At the same time, it also reduces the impact of the external environment such as terrain undulations on the same plot of land. The classification accuracy based on SNIC is much higher than that based on pixels before 15 August, as shown in Figure 8. It shows that the object-based classification method can effectively improve the classification accuracy in the early stage of rice. After 15 August (including 15 August), SNIC-based OA is about 2–3% higher than pixel-based OA. The main reason for this slight improvement is that object-based classification mainly eliminates some artifacts. The VH-sum feature makes the spectral values of rice in the same plot smoother through the accumulation of VH backscattering intensity. This has a certain improvement effect on the missed classification caused by differences within rice categories and the misclassification caused by broken patches in some low-lying dryland areas.

The YCP and XCP datasets are based on the pixel classification of optical data, and the ARM-SARFS method is based on the pixel classification of SAR data. It can also be seen from its spatial distribution of rice that the ARM-SARFS YCP and XCP datasets have a large number of fragmented patches in the dry crop areas in the northeast and southwest regions of the study area. In the classification results of PFO-HKMAR combined with SAR+SI on 31 August, broken patches are also observed in dry crop areas based on pixel classification (Figure 14). Moreover, small water bodies are easily affected by mixed pixels and may be misjudged as rice. The SNIC-based classification does not have this phenomenon at all. The Heilongjiang and Songhua Rivers are affected by seasonal changes in water volume and mixed pixels, resulting in a large amount of debris in the channels based on pixel classification. However, the SNIC-based classification can completely remove water bodies. In summary, the object-based classification method can completely solve the debris in water areas caused by SAR and reduce debris in low-lying dryland areas.

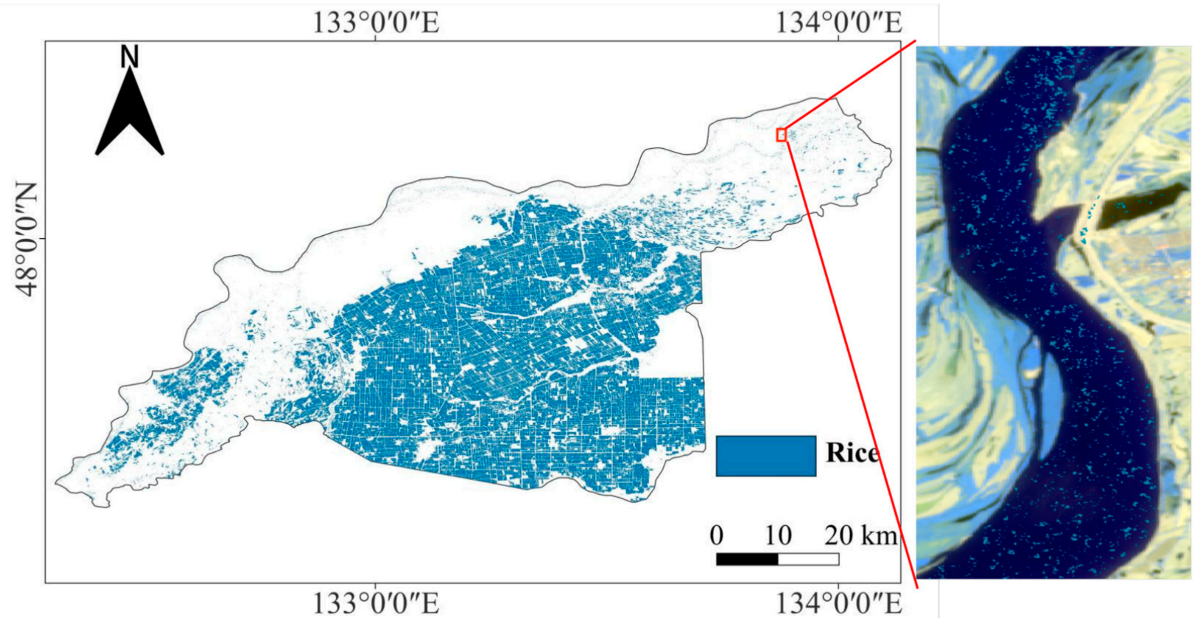

Figure 14. Pixel-based spatial distribution map of rice. (Data: SAR+SI, Date: 31 August.)

5.3. Combination of SI and SAR

This section primarily discusses the impact of different data sources on rice mapping at each step in the PFO-HKMAR method. The classification of optical images is more robust than that of SAR images, as optical images contain a greater amount of spectral information [30]. The flooding signal in rice fields is an important feature for identifying rice, and this feature typically persists for about 2 months [65]. Using time-series optical images is an effective method for accurately identifying rice. However, the study area experiences limited availability of clear optical images due to the onset of the rainy season in July. SAR data can make up for the lack of clear images in optical images during cloudy and rainy periods, improving the generalization and adaptability of rice identification. Additionally, the combination of optical and SAR can capture different aspects of rice's phenological characteristics. Blaes et al. argued that the highest separability of land cover is achieved when optical and SAR images are used together [66]. Yang et al. research shows that although the overall accuracy of Sentinel-2 is significantly higher than VV, VH, or VV+VH, the combined use of optics and SAR images is better than using only optical or SAR images [30]. Integrating images from different sensors and combining the advantages of various data sources can effectively overcome the limitations of a single data source and enhance the accuracy of rice identification [58]. The combined classification accuracy of SAR+SI is higher than that of using only SAR for the SNIC-based classification method, as shown in Figure 9. However, the improvement in accuracy is not significant. This is mainly because the SNIC-based method increases the separability of low-lying dryland areas from rice by averaging all pixels within the object, effectively reducing fragmentation in the classification results. Although the SNIC method can reduce the debris in low-lying areas of dryland, the accuracy of early-season rice mapping can be effectively improved by adding SI features. Although the statistical significance is not great, it can effectively solve the shortcomings of SAR data and avoid the misclassification of dryland low-lying areas and wetlands, which has important practical significance. This study analyzed the performance of rice in different phenological stages and used the hierarchical K-Means binary classification method to identify rice in two steps. The following analysis considers the impact of different data sources on rice identification at each step.

In the first step, K-Means binary classification is performed based on the performance of VH-sum and SI-W for different land cover types. The main purpose is to completely remove buildings, forest land, and other crops, including some wetlands, to obtain a Water-Rice area. The VH-slope feature is not used in this step because the maximum value of the JM distance between rice and other crops is only 1.0 in the VH-slope characteristics during different time intervals throughout the SART2 period. It can also be observed from Section 4.4 that the ARM-SARFS method uses the "V" shaped characteristics before and after the rice transplanting period to identify rice. However, due to different rice planting modes and the coarse time resolution of Sentinel-1B, a large number of points are missed in small farmer economic areas. Therefore, we did not select VH-slope characteristics (including the declining slope of rice before transplanting and the rising slope of rice during the growth stage) in the first step. It can be observed from area 1 in Figure 15 that VH-sum is sensitive to soil moisture and can easily misjudge other crops in low-lying areas as rice. Optical images have shorter wavelengths and provide rich spectral information. The combination of SAR and SI can effectively prevent other crops in low-lying areas from being misjudged as rice. The VH-sum characteristics of rice and wetlands remain consistent in August due to the influence of rainfall. It can be observed from area 2 in Figure 15 that due to the complex spectral information of the built area, the SI-W feature easily misjudges the built area as a water body. The interference of built-up areas has always been a challenging aspect in the study of water extraction [67]. The combination of SAR and SI can not only remove large areas of wetland, but also effectively solve the interference in low-lying dryland areas, completely avoiding misjudgment of built-up areas as rice caused by SI. After comprehensively analyzing the distribution, in the first step, the combination of SAR and SI can completely remove buildings, woodland, and other crops, including large wetlands, to achieve the desired effect.

The second step of PFO-HKMAR using the VH-slope feature to remove water bodies and part of wetlands in the Water-Rice area to obtain a rice distribution map in the study area. Regarding the VH-slope characteristics of the SART2 time stage, as the date increases, the JM distance between rice and water bodies gradually increases and tends to reach a plateau on 15 August. In terms of VH-sum characteristics, the JM distance value between rice and water gradually increased, reaching a maximum of 1.82 on 30 September. A large number of studies have used NDVI to distinguish vegetation and other land cover types [10]. During the rice sowing and transplanting periods, the NDVI value of rice fields closely resembles that of water bodies. As rice grows, the NDVI value gradually increases and reaches the maximum value at the heading stage [15]. Therefore, we conducted a comparative analysis of the VH-slope, VH-sum, and NDVI-mean on 31 August in the SART2 time stage to determine which feature better removes water bodies and wetlands in the Water-Rice area. As shown in the local details of Figure 16, in the Heilongjiang and Songhua River basins, the VH-sum and NDVI-mean features form elongated patches at the boundaries of water bodies, and it is difficult to remove small water bodies. This is mainly caused by the influence of mixed pixels and the seasonal changes in water body boundaries and small water bodies. Moreover, the VH-sum and NDVI-mean features cannot remove the wetlands left over from the first step, such as the wetlands in the Yalu River Basin and Honghe National Nature Reserve that are misjudged as rice. The VH-slope feature can perfectly solve the above problems.

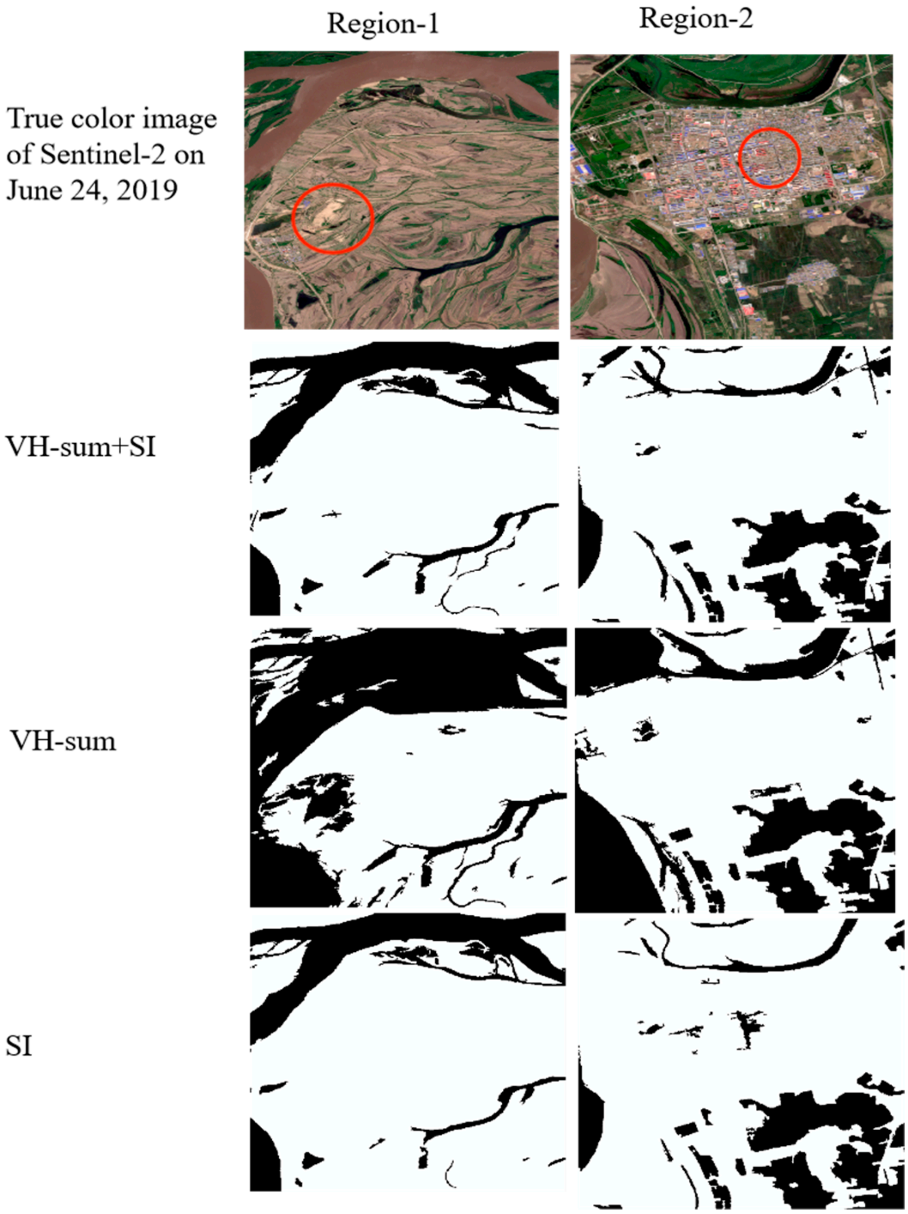

Figure 15. The Water-Rice map of different regions of the study area is based on different characteristics.

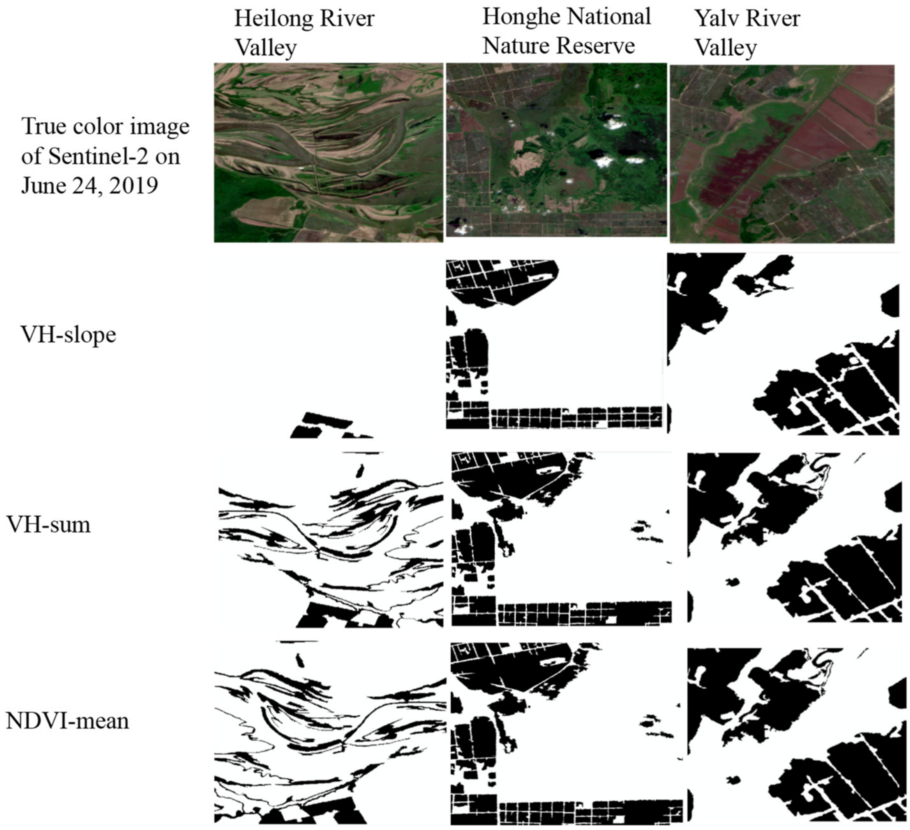

Figure 16. The rice map of different regions of the study area is based on different characteristics.

5.4. Uncertainty and Implication for Future Studies

Although the current results demonstrate the high accuracy of PFO-HKMAR, we recognized that there are still some potential limitations. PFO-HKMAR may be affected by the floods in August, causing the rice covered by floods to lose points. However, PFO-HKMAR can also achieve better results on 31 July before the floods, with OA reaching 0.8833. Moreover, the dunes in the Qinglong River irrigation canal are misdivided into rice fields, which deserves further research. Currently, Northeast China is experimenting with the use of direct seeding drip irrigation technology for rice cultivation. This aspect should be focused on in future rice mapping. The first step of PFO-HKMAR primarily uses the water body information in the early stage of rice growth to determine the Water-Rice area. It can achieve better results during this initial phase. However, the second step requires the slope of the long-term VH backscatter intensity during the rice growth stage to distinguish between rice and water bodies, which is the main reason for the EIT time delay. In the future, spectral changes in different land cover types before rice transplantation can be studied for achieve early identification of rice and water bodies. However, spectral consistency caused by early snow cover in Northeast China and spectral changes caused by snow melting need to be considered. Unlike ARM-SARFS, PFO-HKMAR does not require precise rice transplanting dates. However, it is also necessary to provide the approximate growth period of rice in the study area. This limits the application of PFO-HKMAR in areas and large areas where rice phenological information is unknown. In the future, the spectral time series change information of rice can be used to automatically identify the key phenological stages of rice [68]. This will also help to apply the method in multi-cropping rice growing areas in southern China. Currently, due to incomplete Sentinel-1A data in the study area, we are only using Sentinel-1B images with a temporal resolution of 12 days covering the study area. In addition, other SAR sensor data (such as GF-3 and RADARSAT, etc.) can be supplemented to enhance the density of time series datasets [69]. The Harmonized Landsat Sentinel-2 (HLS) project provides consistent surface reflectance data from the Operational Land Image aboard the joint NASA/USGS Landsat 8 satellite and the Multi-Spectral Instrument aboard Europe's Copernicus Sentinel-2A and Sentinel-2B satellites. The combined measurement enables global land observations every 2–3 days at a spatial resolution of 30 m [70]. However, when we submitted the article in November 2023, although the GEE platform provided the HLS datasets, they were incomplete. The GEE platform is currently improving the HLS datasets.

6. Conclusions

Combining SAR and optical data, this study proposed a hierarchical K-Means binary automatic rice classification method based on phenological information feature optimization (PFO-HKMAR). This method considered characteristics of Sentinel-1B VH backscatter intensity time series for different land cover types and different rice planting patterns. We tested the performance of this method in Tongjiang City, Heilongjiang Province, which has strong spatial heterogeneity, and compared it with two published datasets and ARM-SARFS. The results showed that PFO-HKMAR can realize early-season rice mapping one month in advance. The spatial distribution of rice was consistent with existing data products. OA, KC, and F1 reach 0.9114, 0.8240, and 0.9120, respectively, which are better scores than those of the other three methods. Early-season rice mapping enables governments to make effective decisions on food security issues. In addition, the SAR time series data filtering method that combines average value and SG can achieve near real-time SAR time series filtering in the early or middle stages of rice. The constructed VH-sum characteristics can reflect the dynamic characteristics of rice growth. SNIC segmentation for SI-W based on multiple synthesis methods, multiple spectral indices, and multi-source optical data, solved the problem of image missing and cloud pollution during the rice transplanting period. At the same time, the integrity and homogeneity of rice fields are also improved. It was proved that multiple heterogeneous data sources can complement each other's advantages. The object-oriented classification method can effectively improve the accuracy and time of early-season rice mapping. More detailed spatial information can be provided than the XCP rice spatial distribution map using Landsat data. In summary, PFO-HKMAR can realize early automatic mapping of rice and can be promoted in Northeast China. Future improvements to PFO-HKMAR should focus on the automatic identification of rice phenological stages and its application in multi-season rice areas.

Supplementary Materials: The following supporting information can be downloaded at: https://www.mdpi.com/article/10.3390/rs16020277/s1, Table S1: OA, UA, PA, Kappa, and F1 scores of rice classification based on SNIC and pixel under SAR+SI data source at different time intervals in the SART3 time stage; Table S2: OA, UA, PA, Kappa, and F1 scores of rice classification based on SNIC and pixel under SAR data source at different time intervals in the SART3 time stage; Table S3: Glossary of full-text abbreviations; Table S4: Detailed steps of hierarchical K-Means binary classification method.

Author Contributions: Conceptualization, G.W.; methodology, G.W. and D.M.; data curation, G.W. and D.M.; formal analysis, R.C.; investigation, G.W.; validation, G.W. and D.M.; writing—original draft preparation, G.W.; writing—review and editing, R.C., H.J., X.G. and H.F.; visualization, D.M.; supervision, H.F. and L.W.; project administration, G.Y.; funding acquisition, H.F. All authors have read and agreed to the published version of the manuscript.

Funding: The National Key Research and Development Program of China (2022YFD2001104, 2022YFD2001105).

Data Availability Statement: Sentinel1/2 and Landsat 7/8 data are openly available via the Google Earth Engine (https://earthengine.google.com, accessed on 20 August 2023). Additional data supporting the results of this study can be obtained from the first author (Gengze Wang, gzwang2023@126.com) upon reasonable request.

Acknowledgments: We wish to express our gratitude to ESA and USGS for providing rich remote-sensing images. We wish to express our gratitude to the GEE platform for providing rich computing resources.

Conflicts of Interest: The authors declare no conflicts of interest.

References

1. Kuenzer, C.; Knauer, K. Remote sensing of rice crop areas. *Int. J. Remote Sens.* **2013**, *34*, 2101–2139. [CrossRef]
2. Zheng, H.; Cheng, T.; Yao, X.; Deng, X.; Tian, Y.; Cao, W.; Zhu, Y. Detection of rice phenology through time series analysis of ground-based spectral index data. *Field Crops Res.* **2016**, *198*, 131–139. [CrossRef]
3. Mosleh, M.K.; Hassan, Q.K.; Chowdhury, E.H. Application of remote sensors in mapping rice area and forecasting its production: A review. *Sensors* **2015**, *15*, 769–791. [CrossRef]
4. Chauhan, S.; Darvishzadeh, R.; Lu, Y.; Boschetti, M.; Nelson, A. Understanding wheat lodging using multi-temporal Sentinel-1 and Sentinel-2 data. *Remote Sens. Environ.* **2020**, *243*, 111804. [CrossRef]
5. Skakun, S.; Franch, B.; Vermote, E.; Roger, J.-C.; Becker-Reshef, I.; Justice, C.; Kussul, N. Early season large-area winter crop mapping using MODIS NDVI data, growing degree days information and a Gaussian mixture model. *Remote Sens. Environ.* **2017**, *195*, 244–258. [CrossRef]
6. Cai, Y.; Guan, K.; Peng, J.; Wang, S.; Seifert, C.; Wardlow, B.; Li, Z. A high-performance and in-season classification system of field-level crop types using time-series Landsat data and a machine learning approach. *Remote Sens. Environ.* **2018**, *210*, 35–47. [CrossRef]
7. Defourny, P.; Bontemps, S.; Bellemans, N.; Cara, C.; Dedieu, G.; Guzzonato, E.; Hagolle, O.; Inglada, J.; Nicola, L.; Rabaute, T. Near real-time agriculture monitoring at national scale at parcel resolution: Performance assessment of the Sen2-Agri automated system in various cropping systems around the world. *Remote Sens. Environ.* **2019**, *221*, 551–568. [CrossRef]
8. Zhang, C.; Di, L.; Hao, P.; Yang, Z.; Lin, L.; Zhao, H.; Guo, L. Rapid in-season mapping of corn and soybeans using machine-learned trusted pixels from Cropland Data Layer. *Int. J. Appl. Earth Obs. Geoinf.* **2021**, *102*, 102374. [CrossRef]
9. Dong, J.; Xiao, X. Evolution of regional to global paddy rice mapping methods: A review. *ISPRS J. Photogramm. Remote Sens.* **2016**, *119*, 214–227. [CrossRef]
10. Xuan, F.; Dong, Y.; Li, J.; Li, X.; Su, W.; Huang, X.; Huang, J.; Xie, Z.; Li, Z.; Liu, H. Mapping crop type in Northeast China during 2013–2021 using automatic sampling and tile-based image classification. *Int. J. Appl. Earth Obs. Geoinf.* **2023**, *117*, 103178. [CrossRef]
11. Zhang, C.; Zhang, H.; Tian, S. Phenology-assisted supervised paddy rice mapping with the Landsat imagery on Google Earth Engine: Experiments in Heilongjiang Province of China from 1990 to 2020. *Comput. Electron. Agric.* **2023**, *212*, 108105. [CrossRef]
12. Belgiu, M.; Csillik, O. Sentinel-2 cropland mapping using pixel-based and object-based time-weighted dynamic time warping analysis. *Remote Sens. Environ.* **2018**, *204*, 509–523. [CrossRef]
13. Dong, J.; Xiao, X.; Kou, W.; Qin, Y.; Zhang, G.; Li, L.; Jin, C.; Zhou, Y.; Wang, J.; Biradar, C. Tracking the dynamics of paddy rice planting area in 1986–2010 through time series Landsat images and phenology-based algorithms. *Remote Sens. Environ.* **2015**, *160*, 99–113. [CrossRef]
14. Oliphant, A.J.; Thenkabail, P.S.; Teluguntla, P.; Xiong, J.; Gumma, M.K.; Congalton, R.G.; Yadav, K. Mapping cropland extent of Southeast and Northeast Asia using multi-year time-series Landsat 30-m data using a random forest classifier on the Google Earth Engine Cloud. *Int. J. Appl. Earth Obs. Geoinf.* **2019**, *81*, 110–124. [CrossRef]
15. Ni, R.; Tian, J.; Li, X.; Yin, D.; Li, J.; Gong, H.; Zhang, J.; Zhu, L.; Wu, D. An enhanced pixel-based phenological feature for accurate paddy rice mapping with Sentinel-2 imagery in Google Earth Engine. *ISPRS J. Photogramm. Remote Sens.* **2021**, *178*, 282–296. [CrossRef]
16. Wei, P.; Ye, H.; Qiao, S.; Liu, R.; Nie, C.; Zhang, B.; Song, L.; Huang, S. Early Crop Mapping Based on Sentinel-2 Time-Series Data and the Random Forest Algorithm. *Remote Sens.* **2023**, *15*, 3212. [CrossRef]
17. Blickensdörfer, L.; Schwieder, M.; Pflugmacher, D.; Nendel, C.; Erasmi, S.; Hostert, P. Mapping of crop types and crop sequences with combined time series of Sentinel-1, Sentinel-2 and Landsat 8 data for Germany. *Remote Sens. Environ.* **2022**, *269*, 112831. [CrossRef]
18. Zhou, Y.; Xiao, X.; Qin, Y.; Dong, J.; Zhang, G.; Kou, W.; Jin, C.; Wang, J.; Li, X. Mapping paddy rice planting area in rice-wetland coexistent areas through analysis of Landsat 8 OLI and MODIS images. *Int. J. Appl. Earth Obs. Geoinf.* **2016**, *46*, 1–12. [CrossRef]
19. Xun, L.; Zhang, J.; Cao, D.; Yang, S.; Yao, F. A novel cotton mapping index combining Sentinel-1 SAR and Sentinel-2 multispectral imagery. *ISPRS J. Photogramm. Remote Sens.* **2021**, *181*, 148–166. [CrossRef]
20. Woźniak, E.; Rybicki, M.; Kofman, W.; Aleksandrowicz, S.; Wojtkowski, C.; Lewiński, S.; Bojanowski, J.; Musiał, J.; Milewski, T.; Slesiński, P. Multi-temporal phenological indices derived from time series Sentinel-1 images to country-wide crop classification. *Int. J. Appl. Earth Obs. Geoinf.* **2022**, *107*, 102683. [CrossRef]
21. Xiao, X.; Boles, S.; Frolking, S.; Salas, W.; Moore Iii, B.; Li, C.; He, L.; Zhao, R. Observation of flooding and rice transplanting of paddy rice fields at the site to landscape scales in China using VEGETATION sensor data. *Int. J. Remote Sens.* **2002**, *23*, 3009–3022. [CrossRef]
22. Jiang, X.; Luo, S.; Gao, S.; Fang, S.; Wang, Y.; Yang, K.; Xiong, Q.; Li, Y. An automatic rice mapping method based on constrained feature matching exploiting Sentinel-1 data for arbitrary length time series. *Int. J. Appl. Earth Obs. Geoinf.* **2022**, *114*, 103032. [CrossRef]
23. Zhan, P.; Zhu, W.; Li, N. An automated rice mapping method based on flooding signals in synthetic aperture radar time series. *Remote Sens. Environ.* **2021**, *252*, 112112. [CrossRef]

24. Phan, H.; Le Toan, T.; Bouvet, A. Understanding dense time series of Sentinel-1 backscatter from rice fields: Case study in a province of the Mekong Delta, Vietnam. *Remote Sens.* **2021**, *13*, 921. [CrossRef]
25. Cai, Y.; Lin, H.; Zhang, M. Mapping paddy rice by the object-based random forest method using time series Sentinel-1/Sentinel-2 data. *Adv. Space Res.* **2019**, *64*, 2233–2244. [CrossRef]
26. Ma, X.; Huang, Z.; Zhu, S.; Fang, W.; Wu, Y. Rice Planting Area Identification Based on Multi-Temporal Sentinel-1 SAR Images and an Attention U-Net Model. *Remote Sens.* **2022**, *14*, 4573. [CrossRef]
27. Xu, S.; Zhu, X.; Chen, J.; Zhu, X.; Duan, M.; Qiu, B.; Wan, L.; Tan, X.; Xu, Y.N.; Cao, R. A robust index to extract paddy fields in cloudy regions from SAR time series. *Remote Sens. Environ.* **2023**, *285*, 113374. [CrossRef]
28. Sun, C.; Zhang, H.; Ge, J.; Wang, C.; Li, L.; Xu, L. Rice mapping in a subtropical hilly region based on sentinel-1 time series feature analysis and the dual branch BiLSTM model. *Remote Sens.* **2022**, *14*, 3213. [CrossRef]
29. Makinde, E.O.; Salami, A.T.; Olaleye, J.B.; Okewusi, O.C. Object based and pixel based classification using rapideye satellite imager of ETI-OSA, Lagos, Nigeria. *Geoinform. FCE CTU* **2016**, *15*, 59–70. [CrossRef]
30. Yang, L.; Wang, L.; Abubakar, G.A.; Huang, J. High-resolution rice mapping based on SNIC segmentation and multi-source remote sensing images. *Remote Sens.* **2021**, *13*, 1148. [CrossRef]
31. Wei, P.; Chai, D.; Huang, R.; Peng, D.; Lin, T.; Sha, J.; Sun, W.; Huang, J. Rice mapping based on Sentinel-1 images using the coupling of prior knowledge and deep semantic segmentation network: A case study in Northeast China from 2019 to 2021. *Int. J. Appl. Earth Obs. Geoinf.* **2022**, *112*, 102948. [CrossRef]
32. You, N.; Dong, J.; Li, J.; Huang, J.; Jin, Z. Rapid early-season maize mapping without crop labels. *Remote Sens. Environ.* **2023**, *290*, 113496. [CrossRef]
33. Chen, B.; Xu, B.; Zhu, Z.; Yuan, C.; Suen, H.P.; Guo, J.; Xu, N.; Li, W.; Zhao, Y.; Yang, J. Stable classification with limited sample: Transferring a 30-m resolution sample set collected in 2015 to mapping 10-m resolution global land cover in 2017. *Sci. Bull.* **2019**, *64*, 3.
34. You, N.; Dong, J. Examining earliest identifiable timing of crops using all available Sentinel 1/2 imagery and Google Earth Engine. *ISPRS J. Photogramm. Remote Sens.* **2020**, *161*, 109–123. [CrossRef]
35. Fatchurrachman; Rudiyanto; Soh, N.C.; Shah, R.M.; Giap, S.G.E.; Setiawan, B.I.; Minasny, B. High-Resolution Mapping of Paddy Rice Extent and Growth Stages across Peninsular Malaysia Using a Fusion of Sentinel-1 and 2 Time Series Data in Google Earth Engine. *Remote Sens.* **2022**, *14*, 1875. [CrossRef]
36. Maldonado, S.; Carrizosa, E.; Weber, R. Kernel penalized k-means: A feature selection method based on kernel k-means. *Inf. Sci.* **2015**, *322*, 150–160. [CrossRef]
37. MacQueen, J. Some methods for classification and analysis of multivariate observations. In Proceedings of the Fifth Berkeley Symposium on Mathematical Statistics and Probability, Davis, CA, USA, 21 June–18 July 1965; University of California Press: Berkeley, CA, USA, 1967; pp. 281–297.
38. You, N.; Dong, J.; Huang, J.; Du, G.; Zhang, G.; He, Y.; Yang, T.; Di, Y.; Xiao, X. The 10-m crop type maps in Northeast China during 2017–2019. *Sci. Data* **2021**, *8*, 41. [CrossRef]
39. Beck, P.S.; Atzberger, C.; Høgda, K.A.; Johansen, B.; Skidmore, A.K. Improved monitoring of vegetation dynamics at very high latitudes: A new method using MODIS NDVI. *Remote Sens. Environ.* **2006**, *100*, 321–334. [CrossRef]
40. Roerink, G.; Menenti, M.; Verhoef, W. Reconstructing cloudfree NDVI composites using Fourier analysis of time series. *Int. J. Remote Sens.* **2000**, *21*, 1911–1917. [CrossRef]
41. Gir, R.; Jain, L.; Rai, R. Speckle reduction of synthetic aperture radar images using median filter and savitzky-golay filter. *Int. J. Comput. Appl.* **2015**, *113*, 38–43. [CrossRef]
42. Chen, J.; Jönsson, P.; Tamura, M.; Gu, Z.; Matsushita, B.; Eklundh, L. A simple method for reconstructing a high-quality NDVI time-series data set based on the Savitzky–Golay filter. *Remote Sens. Environ.* **2004**, *91*, 332–344. [CrossRef]
43. Zhang, M.; Lin, H. Object-based rice mapping using time-series and phenological data. *Adv. Space Res.* **2019**, *63*, 190–202. [CrossRef]
44. Xu, J.; Zhu, Y.; Zhong, R.; Lin, Z.; Xu, J.; Jiang, H.; Huang, J.; Li, H.; Lin, T. DeepCropMapping: A multi-temporal deep learning approach with improved spatial generalizability for dynamic corn and soybean mapping. *Remote Sens. Environ.* **2020**, *247*, 111946. [CrossRef]
45. Cao, R.; Chen, Y.; Shen, M.; Chen, J.; Zhou, J.; Wang, C.; Yang, W. A simple method to improve the quality of NDVI time-series data by integrating spatiotemporal information with the Savitzky-Golay filter. *Remote Sens. Environ.* **2018**, *217*, 244–257. [CrossRef]
46. Lee, J.-S.; Wen, J.-H.; Ainsworth, T.L.; Chen, K.-S.; Chen, A.J. Improved sigma filter for speckle filtering of SAR imagery. *IEEE Trans. Geosci. Remote Sens.* **2008**, *47*, 202–213.
47. Nguyen, D.B.; Gruber, A.; Wagner, W. Mapping rice extent and cropping scheme in the Mekong Delta using Sentinel-1A data. *Remote Sens. Lett.* **2016**, *7*, 1209–1218. [CrossRef]
48. Foga, S.; Scaramuzza, P.L.; Guo, S.; Zhu, Z.; Dilley, R.D., Jr.; Beckmann, T.; Schmidt, G.L.; Dwyer, J.L.; Hughes, M.J.; Laue, B. Cloud detection algorithm comparison and validation for operational Landsat data products. *Remote Sens. Environ.* **2017**, *194*, 379–390. [CrossRef]
49. Oreopoulos, L.; Wilson, M.J.; Várnai, T. Implementation on Landsat data of a simple cloud-mask algorithm developed for MODIS land bands. *IEEE Geosci. Remote Sens. Lett.* **2011**, *8*, 597–601. [CrossRef]

50. Son, N.-T.; Chen, C.-F.; Chen, C.-R.; Toscano, P.; Cheng, Y.-S.; Guo, H.-Y.; Syu, C.-H. A phenological object-based approach for rice crop classification using time-series Sentinel-1 Synthetic Aperture Radar (SAR) data in Taiwan. *Int. J. Remote Sens.* **2021**, *42*, 2722–2739. [CrossRef]
51. Wang, L.; Ma, H.; Li, J.; Gao, Y.; Fan, L.; Yang, Z.; Yang, Y.; Wang, C. An automated extraction of small-and middle-sized rice fields under complex terrain based on SAR time series: A case study of Chongqing. *Comput. Electron. Agric.* **2022**, *200*, 107232. [CrossRef]
52. Xiao, X.; Boles, S.; Liu, J.; Zhuang, D.; Frolking, S.; Li, C.; Salas, W.; Moore, B., III. Mapping paddy rice agriculture in southern China using multi-temporal MODIS images. *Remote Sens. Environ.* **2005**, *95*, 480–492. [CrossRef]
53. Xu, H. A study on information extraction of water body with the modified normalized difference water index (MNDWI). *J. Remote Sens.* **2005**, *9*, 595.
54. Wang, X.; Xie, S.; Zhang, X.; Chen, C.; Guo, H.; Du, J.; Duan, Z. A robust Multi-Band Water Index (MBWI) for automated extraction of surface water from Landsat 8 OLI imagery. *Int. J. Appl. Earth Obs. Geoinf.* **2018**, *68*, 73–91. [CrossRef]
55. Jiang, Z.; Huete, A.R.; Chen, J.; Chen, Y.; Li, J.; Yan, G.; Zhang, X. Analysis of NDVI and scaled difference vegetation index retrievals of vegetation fraction. *Remote Sens. Environ.* **2006**, *101*, 366–378. [CrossRef]
56. Yin, Q.; Liu, M.; Cheng, J.; Ke, Y.; Chen, X. Mapping paddy rice planting area in northeastern China using spatiotemporal data fusion and phenology-based method. *Remote Sens.* **2019**, *11*, 1699. [CrossRef]
57. Schmidt, K.; Skidmore, A. Spectral discrimination of vegetation types in a coastal wetland. *Remote Sens. Environ.* **2003**, *85*, 92–108. [CrossRef]
58. Jiang, Q.; Tang, Z.; Zhou, L.; Hu, G.; Deng, G.; Xu, M.; Sang, G. Mapping Paddy Rice Planting Area in Dongting Lake Area Combining Time Series Sentinel-1 and Sentinel-2 Images. *Remote Sens.* **2023**, *15*, 2794. [CrossRef]
59. Griffiths, P.; Nendel, C.; Hostert, P. Intra-annual reflectance composites from Sentinel-2 and Landsat for national-scale crop and land cover mapping. *Remote Sens. Environ.* **2019**, *220*, 135–151. [CrossRef]
60. Jia, S.; Zhan, Z.; Zhang, M.; Xu, M.; Huang, Q.; Zhou, J.; Jia, X. Multiple feature-based superpixel-level decision fusion for hyperspectral and LiDAR data classification. *IEEE Trans. Geosci. Remote Sens.* **2020**, *59*, 1437–1452. [CrossRef]
61. Achanta, R.; Susstrunk, S. Superpixels and polygons using simple non-iterative clustering. In Proceedings of the Proceedings of the IEEE Conference on Computer Vision and Pattern Recognition, Honolulu, HI, USA, 21–26 July 2017; pp. 4651–4660.
62. Ali, I.; Rehman, A.U.; Khan, D.M.; Khan, Z.; Shafiq, M.; Choi, J.-G. Model selection using K-means clustering algorithm for the symmetrical segmentation of remote sensing datasets. *Symmetry* **2022**, *14*, 1149. [CrossRef]
63. Ren, Z.; Sun, L.; Zhai, Q. Improved k-means and spectral matching for hyperspectral mineral mapping. *Int. J. Appl. Earth Obs. Geoinf.* **2020**, *91*, 102154. [CrossRef]
64. Yang, H.; Pan, B.; Wu, W.; Tai, J. Field-based rice classification in Wuhua county through integration of multi-temporal Sentinel-1A and Landsat-8 OLI data. *Int. J. Appl. Earth Obs. Geoinf.* **2018**, *69*, 226–236. [CrossRef]
65. Lobell, D.B.; Hammer, G.L.; McLean, G.; Messina, C.; Roberts, M.J.; Schlenker, W. The critical role of extreme heat for maize production in the United States. *Nat. Clim. Change* **2013**, *3*, 497–501. [CrossRef]
66. Blaes, X.; Vanhalle, L.; Defourny, P. Efficiency of crop identification based on optical and SAR image time series. *Remote Sens. Environ.* **2005**, *96*, 352–365. [CrossRef]
67. Cordeiro, M.C.; Martinez, J.-M.; Peña-Luque, S. Automatic water detection from multidimensional hierarchical clustering for Sentinel-2 images and a comparison with Level 2A processors. *Remote Sens. Environ.* **2021**, *253*, 112209. [CrossRef]
68. Tian, G.; Li, H.; Jiang, Q.; Qiao, B.; Li, N.; Guo, Z.; Zhao, J.; Yang, H. An Automatic Method for Rice Mapping Based on Phenological Features with Sentinel-1 Time-Series Images. *Remote Sens.* **2023**, *15*, 2785. [CrossRef]
69. Ma, H.; Wang, L.; Sun, W.; Yang, S.; Gao, Y.; Fan, L.; Yang, G.; Wang, Y. A new rice identification algorithm under complex terrain combining multi-characteristic parameters and homogeneous objects based on time series dual-polarization synthetic aperture radar. *Front. Ecol. Evol.* **2023**, *11*, 1093454. [CrossRef]
70. Hu, J.; Chen, Y.; Cai, Z.; Wei, H.; Zhang, X.; Zhou, W.; Wang, C.; You, L.; Xu, B. Mapping Diverse Paddy Rice Cropping Patterns in South China Using Harmonized Landsat and Sentinel-2 Data. *Remote Sens.* **2023**, *15*, 1034. [CrossRef]